

Tunnel field-effect transistors for sensitive terahertz detection

I. Gayduchenko^{1,2*}, S.G. Xu^{3,4*}, G. Alymov^{1*}, M. Moskotin^{1,2}, I. Tretyakov⁵, T. Taniguchi⁶, K. Watanabe⁷, G. Goltsman^{2,8}, A.K. Geim^{3,4}, G. Fedorov^{1,2†}, D. Svintsov^{1†}, and D.A. Bandurin^{1,3,9†}

¹Moscow Institute of Physics and Technology (National Research University), Dolgoprudny 141700, Russia

²Physics Department, Moscow Pedagogical State University, Moscow, 119435, Russia

³School of Physics, University of Manchester, Oxford Road, Manchester M13 9PL, United Kingdom

⁴National Graphene Institute, University of Manchester, Manchester M13 9PL, United Kingdom

⁵Astro Space Center, Lebedev Physical Institute of the Russian Academy of Sciences, Moscow 117997, Russia

⁶International Center for Materials Nanoarchitectonics, National Institute of Material Science, Tsukuba 305-0044, Japan

⁷Research Center for Functional Materials, National Institute of Material Science, Tsukuba 305-0044, Japan

⁸National Research University Higher School of Economics, Moscow, 101000, Russia

⁹Present address: Department of Physics, Massachusetts Institute of Technology, Cambridge, Massachusetts 02139, USA

The rectification of electromagnetic waves to direct currents is a crucial process for energy harvesting, beyond-5G wireless communications, ultra-fast science, and observational astronomy. As the radiation frequency is raised to the sub-terahertz (THz) domain, ac-to-dc conversion by conventional electronics becomes challenging and requires alternative rectification protocols. Here we address this challenge by tunnel field-effect transistors made of bilayer graphene (BLG). Taking advantage of BLG's electrically tunable band structure, we create a lateral tunnel junction and couple it to an antenna exposed to THz radiation. The incoming radiation is then down-converted by the tunnel junction nonlinearity, resulting in high-responsivity (> 4 kV/W) and low-noise (0.2 pW/ $\sqrt{\text{Hz}}$) detection. We demonstrate how switching from intraband Ohmic to interband tunneling regime can raise detectors' responsivity by few orders of magnitude, in agreement with the developed theory. Our work demonstrates a potential application of tunnel transistors for THz detection and reveals BLG as a promising platform therefor.

Field effect transistors (FETs) recently found an unexpected application for the rectification of THz and sub-THz signals beyond their cutoff frequency^{1,2}. This technology paves the way for on-chip³, low-noise⁴, and sub-nanosecond radiation detection^{5,6} offering the possibility of $\gtrsim 10$ Gb/s data transfer rates. Contrary to competing diode rectifiers, FETs offer the possibility of phase-sensitive detection^{7,8} vital for noise-immune communications with phase modulated signals. Recent innovations towards enhanced responsivity of FET-detectors include the use of 2D materials^{9–11}, exotic nonlinearities^{12–16}, enhanced light-matter coupling¹⁷ and plasmonic effects^{18–20}. Despite the rich and complex physics of THz rectification, the responsivity of most FET-detectors is governed by the sensitivity of the channel conductivity G_{ch} to the gate voltage V_g , parameterized via the normalized transconductance $F = -d \ln G_{\text{ch}} / dV_g$ ^{2,21}. The transconductance in conventional FETs has a fundamental limit of $e/k_B T$ (e is the elementary charge and $k_B T$ is the thermal energy) dictated by the leakage of thermal carriers over the gate-induced barrier, termed as 'Boltzmann tyranny'. Although this process is well-recognized as a limiting factor for the minimal power dissipation of FETs in integrated circuits, it has been scarcely realised that it also imposes a bound on the responsivity of antenna-coupled FETs to THz fields.

One of the most promising routes to escape from the Boltzmann tyranny is the manipulation of interband tunneling instead of intraband thermionic currents. This idea is materialized in a tunnel field effect

transistor (TFET)^{22–24}. TFETs find their applications in low-voltage electrical and optical switching²⁵, accelerometry²⁶, chemical²⁷ and biological sensing^{28,29}. In spite of this variety, the use of TFETs for the rectification of high-frequency signals³⁰ has not been attempted so far. This is also surprising considering recent advances in the development of tunnelling high-frequency rectifiers and detectors based on quantum dots^{31,32}, diodes^{33–38} and superconducting tunnel junctions^{39–41}. A possible reason is that low on-state current and cut-off frequency of TFETs stimulate the belief on their inapplicability in teratronics⁴².

In this work, we show that the opposite is true and demonstrate the use of TFETs for highly-sensitive sub-THz and THz detection. Using bilayer graphene (BLG) as a convenient platform for this enquiry, we fabricate a dual-gated TFET and couple it to a broadband THz antenna. The received high-frequency signal is rectified by electrostatically-defined tunnel junction resulting in high-responsivity and low-noise detection. Our experimental results and the developed theory suggest that the origin of the high responsivity in our detectors is not the large transconductance, but rather steep curvature of the tunneling $I - V$ characteristic⁴³. Our findings point out that even TFETs without sub- $k_B T/e$ switching can act as efficient THz rectifiers preserving all the benefits of transistor-based detection technology.

RESULTS

Device fabrication and characterization. For the proof-of-principle demonstration, we constructed a TFET of a BLG taking advantage of its unique electronic properties. BLG is a narrow-band semi-

*Equally contributed authors.

†Corresponding authors: gefedorov@mail.ru, svintcov.da@mipt.ru, bandurin@mit.edu.

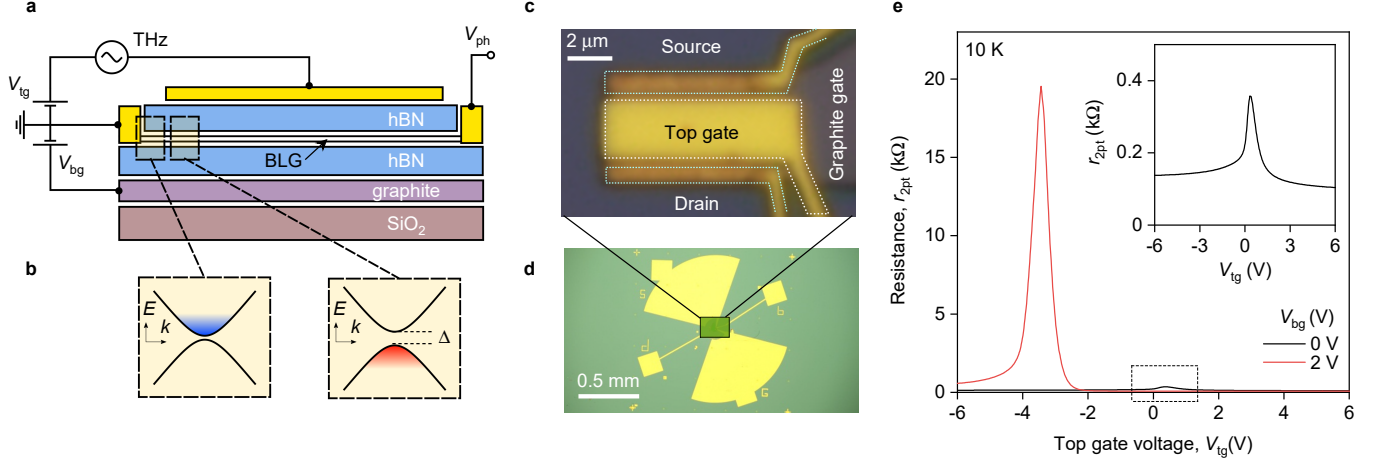


Fig. 1 Dual-gated bilayer graphene THz detector. **a**, Schematic of an hBN encapsulated dual-gated BLG transistor. THz radiation is incident on a broadband antenna connected to the source (S) and gate terminals yielding modulation of the top gate-to-source voltage (V_{tg}) while the back gate voltage (V_{bg}) is fixed. The build-up photovoltage V_{ph} is read out between the source and drain (D) terminals. **b**, Band structure of the BLG at the interface between the n -doped bottom gate-sensitive region and dual-gated p -doped channel (Δ is the band gap). Blue and red colours illustrate conduction and valence bands fillings respectively. Note, even for a single-gated region, a finite band gap appears in the energy dispersion due to the difference in on-site energies between the top and bottom graphene layers⁴⁴. **c-d**, Optical photographs of the fabricated dual-gated detector. The source and top-gate terminals are connected to a broadband bow-tie antenna. **e**, The two-terminal resistance of our BLG device, r_{2pt} , as a function of V_{tg} for two representative $V_{bg} = 0$ and $V_{bg} = 2$ V. Inset: Zoomed-in $r_{2pt}(V_{tg})$ for $V_{bg} = 0$ V. $T = 10$ K.

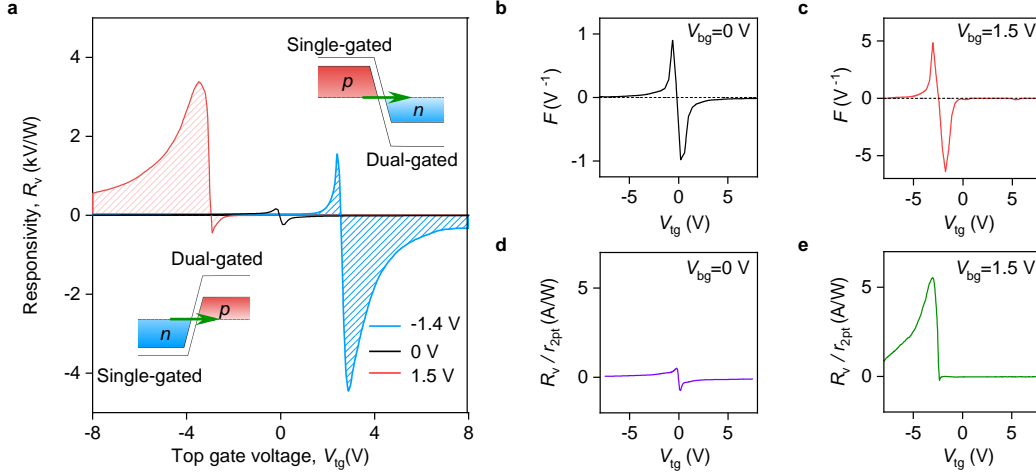


Fig. 2 Tunnelling-assisted THz detection **a**, Detector responsivity, R_v , as a function of V_{tg} for $V_{bg} = 0$ V (black), $V_{bg} = -1.4$ V (blue) and $V_{bg} = 1.5$ V (red) measured in response to $f = 0.13$ THz radiation. $T = 10$ K. Inset illustrates band profiles in the vicinity of the single and dual-gated interface when V_{bg} and V_{tg} are of opposite polarities. Green arrow illustrates interband tunnelling. **b,c** Normalized transconductance F versus V_{tg} obtained by numerical differentiation of the device resistance for $V_{bg} = 0$ V (b) and $V_{bg} = 1.5$ V (c). Note, $F(V_{tg})$ dependencies are fairly symmetric whereas the $R_v(V_{tg})$ is highly asymmetric for the same V_{bg} (a). **d, e** R_v from (a) normalized to the channel resistance r_{2pt} as a function of V_{tg} for given V_{bg} .

conductor characterized by a tunable band structure highly sensitive to the transverse electric field⁴⁴. This ensures a steep ambipolar field effect and allows for an independent control of the band gap size and the carrier density, n ⁴⁵, providing a unique opportunity for a fully electrostatic engineering of the spatial band profile^{46–48}. We employed this property to electrostatically define typical TFET configuration shown in Fig. 1a,b. In addition, BLG hosts a high-mobility electronic system, a crucial property for high-frequency applications. As we now proceed to show, these properties make BLG a convenient platform to demonstrate the drastic differences in performance of intraband field-effect-enabled detection and its interband tunneling counterpart within the same device.

We fabricated our detector by an encapsulation of BLG between two

slabs of hexagonal boron nitride (hBN) using standard dry transfer technique described elsewhere⁴⁹ (See [Methods](#)). The BLG channel of length $L = 2.8 \mu\text{m}$ and width $W = 6.2 \mu\text{m}$ was assembled on top of a relatively thin (~ 10 nm) graphite back gate which ensured efficient screening of remote charge impurities in Si/SiO₂ substrate⁵⁰. The device was also equipped with a second (top) gate electrode deposited symmetrically between the source and drain contacts. Importantly, relatively short ($l < 100$ nm) regions near the contacts were not covered by the top gate and thus were affected by the bottom one only. This configuration allowed us to define a lateral tunnel junction between single- and double-gated regions when the top and bottom gate voltages (V_{tg} and V_{bg} respectively) had opposite polarities^{46–48}, as explained in Figs. 1b and 5.

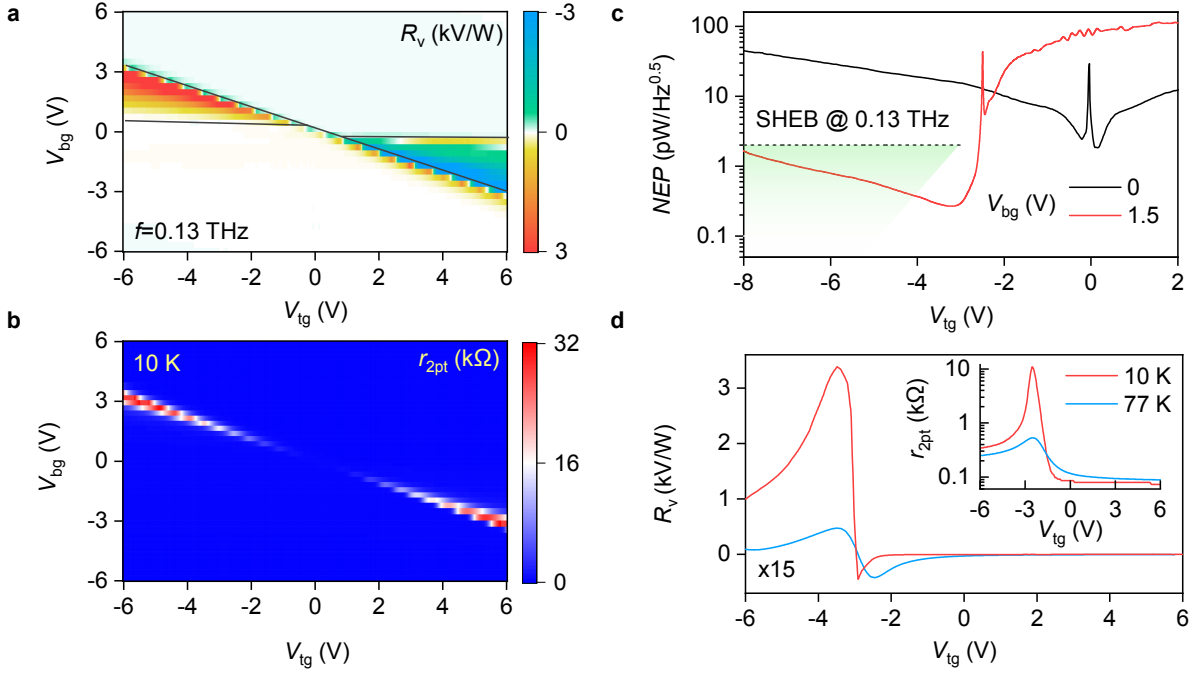


Fig. 3 Performance of the BLG-TFET detector. **a**, Responsivity of our detector as a function of V_{bg} and V_{tg} recorded in response to $f = 0.13$ THz radiation. The black lines demark the (V_{tg}, V_{bg}) regions where the tunnel junction configuration is realized. **b**, $r_{2pt}(V_{tg}, V_{bg})$ map measured at $T = 10$ K. The appearance of highly resistive regions (red) points out to the band gap opening in BLG. **c**, NEP of our detector at given V_{bg} determined using the Johnson–Nyquist relation for the noise spectral density. Horizontal line marks NEP level for SHEBs operating at the same f and $T = 4.2$ K (See [Supplementary Note 3](#) for a detailed comparison of the BLG-TFET with other THz detectors). Green shaded region indicates the spread in NEP for SHEBs at higher f . **d**, Temperature dependence of $R_v(V_{tg})$ and $r_{2pt}(V_{tg})$ (inset) at $V_{bg} = 1.5$ V.

The device was coupled to the incident radiation via broadband bow-tie antenna connected to the source and top gate electrodes. The rectified dc photovoltage, V_{ph} , was read out between the source and drain terminals as shown in Fig. 1a (See [Methods](#)).

Prior to photoresponse measurements, we characterized the transport properties of our device. Figure 1e shows the dependence of our detector’s two-terminal resistance, r_{2pt} , on V_{tg} for two representative values of V_{bg} measured at $T = 10$ K. At $V_{bg} = 0$ V, $r_{2pt}(V_{tg})$ exhibits familiar bell-like structure that peaks at the charge neutrality point (CNP) where $r_{2pt} \approx 0.4$ k Ω (inset of Fig. 1e). Application of $V_{bg} = 2$ V shifts the CNP to negative V_{tg} and results in drastic increase of r_{2pt} that reaches 20 k Ω already at $V_{tg} \approx -3.5$ V. This increase is a clear indicative of the electrically-induced band gap in BLG^{44,45}.

Tunneling-enabled detection. Figure 2a shows the external responsivity of our detector, $R_v = V_{ph}/P_{in}$, as a function of V_{tg} recorded in response to $f = 0.13$ THz radiation. Here V_{ph} is the generated photovoltage and P_{in} is the incident radiation power (See [Methods](#) for the details of responsivity determination). At $V_{bg} = 0$ V, $R_v(V_{tg})$ exhibits a standard antisymmetric sign-changing behaviour with $|R_v|$ reaching 200 V/W close to the CNP. The functional form of $R_v(V_{tg})$ follows that of the normalized transconductance $F = -(dG_{ch}/dV_{tg})/G_{ch}$ (Fig. 2b), where $G_{ch} = 1/r_{2pt}$, and is consistent with previous studies of graphene-based THz detectors^{10,19,51}. This standard behaviour is routinely understood in terms of a combination of resistive self-mixing and photo-thermoelectric rectification, two predominant mechanisms that govern THz detection in graphene-based FETs⁵².

The response of our device changes drastically when a finite vertical electric field is applied perpendicular to the BLG channel. Figure 2a shows the $R_v(V_{tg})$ dependence for $V_{bg} = 1.5$ V and reveals a giant increase of R_v exceeding 3 kV/W (red curve). A notable feature of the observed dependence is its strong asymmetry with respect to zero V_{bg} behaviour: namely, $|R_v|$ is more than an order of magnitude larger for the p -doped channel (to the left from the CNP in Fig. 1e) as compared

to the case of n -doping (to the right from the CNP in Fig. 1e). In addition, while the response decays rapidly with increasing V_{tg} on the n -doped side, a finite R_v is observed over the whole span of V_{tg} at which the channel is p -doped. Furthermore, when the sign of V_{bg} is reversed, $R_v(V_{tg})$ remains asymmetric but, in this case, it is strongly enhanced for positive V_{tg} (blue curve in Fig. 2a). Importantly, the F -factor remains fairly symmetric for the V_{tg}/V_{bg} combinations at which R_v exhibits strong asymmetry. This observation suggests that the strong rectification of THz radiation in our device is not caused by the non-linearities in the dual-gated BLG channel. Moreover, the increase in R_v cannot be explained by a trivial enhancement of channel resistance. To demonstrate this, in Fig. 2d and e we plot R_v normalized to r_{2pt} , a quantity with the dimension of current responsivity. A symmetric $R_v/r_{2pt}(V_{tg})$ dependence measured at $V_{bg} = 0$ V is conceded with amplified and highly-asymmetric curve at finite V_{bg} , thereby excluding resistance-enabled R_v enhancement.

Figure 3a-b details our observations further by showing maps of $R_v(V_{tg}, V_{bg})$ and $r_{2pt}(V_{tg}, V_{bg})$. Enhanced R_v is observed in two distinct quadrants characterized by an anti-symmetric (with respect to the V_{bg}) sign pattern (see [Supplementary Note 1](#) for the line cuts of the map in Fig. 3a). Outside these quadrants, R_v was found negligibly small. Interestingly, r_{2pt} -map is fairly symmetric featuring gradual increase of resistance at the CNP with increasing vertical field as expected for BLG^{44,45}. We have also studied the performance of our detectors at higher f and found consistent highly asymmetric response similar to that shown in Fig. 2b ([Supplementary Note 2](#)) highlighting broadband character of the rectification mechanism. Furthermore, using Johnson–Nyquist relation for the noise spectral density $S = \sqrt{4k_B T r_{2pt}}$, we estimate the noise equivalent power of our detector, $NEP = S/R_v$, to reach 0.2 pW/ $\sqrt{\text{Hz}}$ at $T \approx 10$ K (Fig. 3c). For comparison, commercial superconducting hot electron bolometers (SHEB) operating at lower $T = 4.2$ K feature NEP of 0.1–2 pW/ $\sqrt{\text{Hz}}$ (Fig. 3c, green shaded area) that makes our dual-gated detectors competitive with the commer-

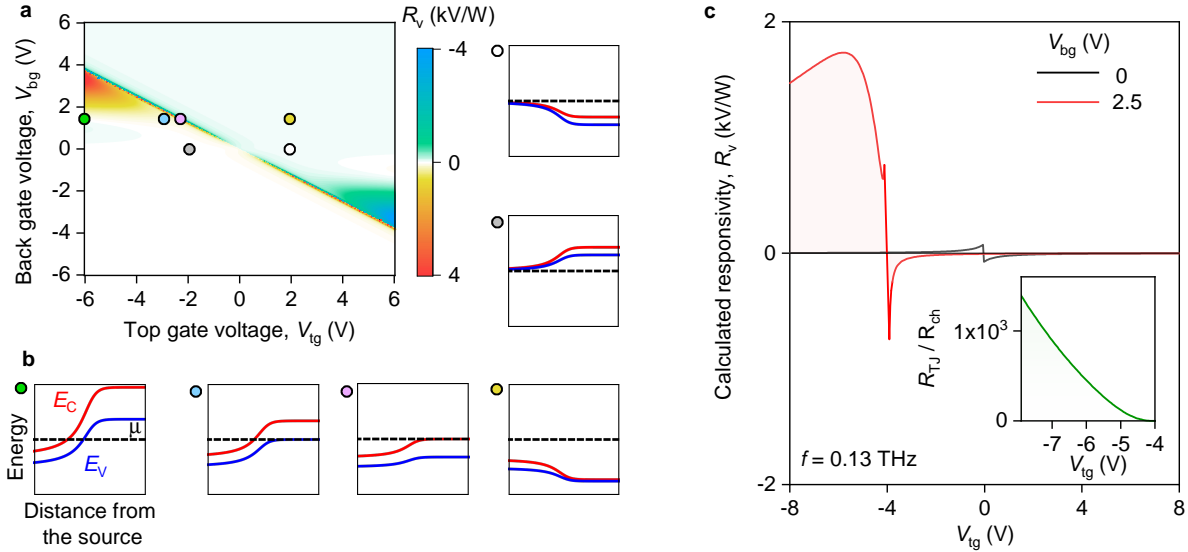


Fig. 4 Modelling tunneling-assisted THz detection. **a**, Calculated $R_v(V_{tg}, V_{bg})$ map of our dual-gated BLG device in response to $f = 0.13$ THz radiation. **b**, Calculated band profiles for different (V_{tg}, V_{bg}) configurations indicated by the colored symbols in (a). White, grey, yellow and pink symbols point to the band diagrams of the FET mode whereas the green and blue symbols correspond to the regime of interband tunnelling. Red, blue and black lines illustrate conduction band minimum (E_C), valence band maximum (E_V), and the chemical potential (μ), respectively. **c**, Line cuts of the map in (a) for $V_{bg} = 0$ V and $V_{bg} = 2.5$ V. The radiation resistance of the antenna $Z_{rad} \approx 75 \Omega$ was used for these calculations (Methods). Inset: The ratio between the tunnel junction, R_{TJ} , contribution to the responsivity and that of the channel nonlinearity, R_{ch} , for $V_{bg} = 2.5$ V.

cial technology. (Supplementary Note 3).

In order to understand deeper the peculiar detection mechanism of our cooled detector, we have studied the temperature dependence of its performance. Figure 3d compares the $R_v(V_{tg})$ dependencies measured at $T = 10$ and 77 K in response to $f = 0.13$ THz radiation. For p -doped channel, $R_v(V_{tg})$ drops by more than 2 orders of magnitude whereas a 10-fold decrease in $R_v(V_{tg})$ is observed for the n -doped side. Furthermore, in contrast to the behaviour observed at 10 K, $R_v(V_{tg})$ curves become more symmetric at liquid nitrogen T . To compare, r_{2pt} at the CNP also drops with increasing T (inset of Fig. 3d), demonstrating usual insulating behaviour of gapped BLG at zero doping. However, r_{2pt} exhibits clear asymmetry with respect to the CNP. In particular, for the case of n -doped channel, r_{2pt} is rather small ($\approx 100 \Omega$) and it grows with increasing T , a signature of phonon-limited transport, whereas on the p -doped side we observed a pronounced decrease of r_{2pt} with increasing T ; r_{2pt} is of the order of $0.5 \text{ k}\Omega$ away from the CNP. The giant enhancement of R_v , insulating T -dependence of r_{2pt} and its increase, when V_{tg} and V_{bg} are of opposite polarities, suggest that the behaviour of our BLG detector is governed by the interband tunneling as we now proceed to demonstrate.

Modelling tunneling-enabled photoresponse. Our dual-gated BLG transistor can be modelled by an equivalent circuit described in Methods (see below). It consists of the gate-controlled channel conductance \tilde{G}_{ch} and tunnel junctions at the source and drain with conductances G_S and G_D , respectively. The net responsivity R_v of such a circuit is the sum of three ‘intrinsic’ responsivities (marked with subscript i) weighted with voltage division factors $\gamma = [1 + G_S/\tilde{G}_{ch}]^{-1}$ and multiplied by a factor of $\approx 4Z_{rad}$ relating the mean square of the antenna’s output voltage with the incident power (Z_{rad} is the radiation resistance of the antenna; exact expression for the prefactor is given in Methods):

$$R_v \approx 4Z_{rad}[R_{TJ,i}|\gamma|^2 + R_{TG,i}\text{Re}\gamma + R_{ch,i}|1-\gamma|^2]. \quad (1)$$

The channel responsivity, $R_{ch,i}$, is proportional to the transconductance²¹ and appears due to resistive self-mixing effect, i.e. due to simultaneous modulation of carrier density by transverse gate field and

their drag by longitudinal field. The tunnel junction responsivity $R_{TJ,i}$ emerges due to non-linear dependence of tunneling current on junction voltage, V_{TJ} . Finally, the responsivity $R_{TG,i}$ appears due to the simultaneous action of the gate voltage that modulates tunnel barrier and junction voltage that pulls the carriers. All three contributions can be calculated from the sensitivities of conductances G_S and \tilde{G}_{ch} to V_{tg} and V_{bg} (Methods and Supplementary Note 4).

Figure 4a plots the results of such calculations in a form of 2D map which shows R_v dependence on V_{tg} and V_{bg} (see Methods and Supplementary Note 4). The map captures well all the features of the experiment, in particular, the asymmetric gate voltage dependence of the responsivity and its giant increase when the voltage of top and bottom gates is of the opposite polarity. This is most clearly visible in Fig. 4c which compares $R_v(V_{tg})$ dependencies for the cases of zero and finite V_{bg} . Moreover, our model indicates a broadband character of the tunneling-assisted photoresponse (Supplementary Note 2) as well as provides a remarkable quantitative agreement with experiment provided that $Z_{rad} \approx 75 \Omega$, a typical value for the antenna of this type^{19,52}.

The peculiar response of our detector can be understood with the band diagrams shown in Fig. 4b. The detector can operate in two regimes: the regime of intraband transport (white, grey, yellow and purple symbols on the map in Fig. 4a) and the regime of interband tunneling (green and blue symbols on the map in Fig. 4a), depending on the gate voltage configuration. At zero V_{bg} , BLG is practically gapless, so that the tunnel barrier between the source and the channel is almost absent (white and grey symbols on the map in Fig. 4a). In this regime, the device responsivity is controlled by $R_{ch,i}$ which exhibits a symmetric dependence on V_{tg} (cf Fig. 4c (black line) and Fig. 2a). On the contrary, when a finite bias is applied to the bottom gate, the tunnel junction is formed as illustrated in Fig. 4b (green and blue symbols). Its intrinsic rectifying capability $R_{TJ,i}$ exceeds that of the transistor channel $R_{ch,i}$, as shown in the inset to Fig. 4c by several orders of magnitude. This stems from an ultra-strong, exponential sensitivity of the tunnel conductance to the voltage at the junction, as compared to the smooth dependence of \tilde{G}_{ch} on V_{tg} . Moreover, the ac voltage being rectified drops almost completely on a weakly conducting junction but not on the well-conducting channel

in the tunneling regime ($|\gamma| \rightarrow 1$). This can be viewed as the 'self-localization' of the ac field in the tunneling rectifier, which contributes to the responsivity enhancement.

Our theory, which successfully describes the response of the BLG device, can also serve to demonstrate the prospects and fundamental limits of TFET-based THz detectors. In the current device, the tunneling is assisted by fluctuations of in-plane electric field induced by local groups of charged impurities⁵³. In ideal devices, the responsivity would exceed 100 kV/W, according to the model calculations (Supplementary Note 5). It is also remarkable that the expected high transconductance of TFET concedes to even higher nonlinearity of the tunnel junction, thus $R_{TJ,i} \gg R_{TG,i}$ in the present and ideal devices. $R_{TG,i}$ can dominate in situations where the source and channel simultaneously possess large gap and remain undoped; thence electron tunneling occurs from a filled valence band of the source to an empty conduction band of the channel in the vicinity of band edges. Large density of states near the bottom of 'Mexican hat'-like spectrum of BLG further increases TFET switching steepness⁵⁴. Realization of such band alignment is possible with the application of the drain bias and/or with extra doping gates.

Last, we point to an important advantage of TFET rectifiers with 2D channels, namely, the low internal capacitance of the lateral tunnel junctions. Up to small logarithmic terms, it is given by⁵⁵ $C_{TJ} = 2W\epsilon\epsilon_0 \approx 0.4$ fF for the device width of $W = 6.2$ μm (as in our experiment) and dielectric environment $\epsilon \approx 4$. The detection cutoff associated with the capacitive shunting of the tunnel junction is therefore expected at $f \sim 1/(2\pi C_{TJ} Z_{\text{rad}}) \sim 5$ THz for $Z_{\text{rad}} \approx 75$ Ω .

DISCUSSION

Despite the fact that our model successfully describes all the features of the observed photoresponse, it does not account for a possible thermoelectric contribution to the responsivity of TFET detectors^{5,10,52}. Assuming that the Seebeck coefficient varies between S_{cont} in the single-gated region near the source contact and S_{ch} in the double-gated channel, one can estimate the thermoelectric contribution as⁵² $R_{\text{TE}} \approx (3e/2\pi^2 k_B)(S_{\text{cont}} - S_{\text{ch}})(e|Z_a|/k_B T)(\delta L/L)$, where δL is the length of single-gated region and L is the full channel length. Together with Mott's formula for Seebeck coefficient $S = (\pi^2 k_B^2 T/3e)d \ln \sigma/dE_F \sim (\pi^2 k_B^2 T/3eE_F)$ this yields R_{TE} of the order of 5...200 V/W for Fermi energies in the range 50...200 meV which is more than two orders of magnitude smaller than the measured responsivity of our TFET detector yet close to that of conventional FET detectors based on gapless monolayer graphene⁵². Thus, the variations of the 'bulk' thermoelectric parameters cannot explain the observed strong and asymmetric photoresponse of our device.

We note, however, that it is rather challenging to test whether the tunnel junction itself acts as a thermoelectric generator or not⁵⁶. The respective thermoelectric coefficient can be estimated as $S_{TJ} \sim (k_B^2 T/e)d \ln G_{TJ}/dV_g$, and its functional dependence on the gate voltage would be indistinguishable from the junction rectification described by our model. In principle, measurements of the electron temperature can elucidate the presence of such rectification mechanism, which is however beyond the scope of our work. Nevertheless, even if present, such a mechanism is also due to the presence of the tunnel junction that substantiates the use of TFETs for sensitive THz detection.

Last but not least, we note that reaching the ultimately-low noise-equivalent power would require impedance matching between antenna and TFET⁵⁷. As the noise power density is proportional to $r_{2\text{pt}}$, and the voltage responsivity saturates at large resistances⁵⁸, we can expect the reduction of noise level by a factor of $[r_{2\text{pt}}/Z_{\text{rad}}]^{1/2}$ in optimized devices. Taking $Z_{\text{rad}} = 75$ Ω and $r_{2\text{pt}} = 1...5$ k Ω at the points of maximum R_v , we anticipate the ultimate NEP to be 3...8 times smaller than that reported in Fig. 3c and Supplementary Figure 3. The simplest way of such matching lies in increasing the device width W .

In conclusion, we have shown an opportunity to use TFETs as high-

responsivity detectors of sub-THz and THz radiation. Constructing a prototypical device from a BLG dual-gated structure and coupling it to a broadband antenna allowed us to demonstrate the drastic difference between a conventional FET-based approach and TFET-enabled rectification. Furthermore, we have developed a full model enabling one to predict the performance of TFET detectors based on the details of their band structure. This model was applied to the case of BLG TFET detector and successfully captured all the experimentally observed features. As an outlook, we note that BLG is just a convenient platform to demonstrate the performance of TFET-based THz detectors. This approach can be extended to larger-gap materials⁵⁹ enabling room-temperature operation, as well as to CMOS-compatible structures⁶⁰. Furthermore, we envision that alternative transistor technologies enabling transconductance beyond Boltzmann limit (phase-change FETs⁶¹, negative capacitance FETs⁶²) would also demonstrate ultra-sensitive THz detection.

METHODS

Device fabrication. To fabricate tunneling-enabled BLG photodetector we first encapsulated BLG between relatively thick hBN crystals using the standard dry-peel technique⁴⁹. The thickness of hBN crystals was measured by atomic force microscopy. The stack was then transferred on top of a predefined back gate electrode made of graphite deposited onto a low-conductivity THz-transparent silicon wafer capped with a thin oxide layer (500 nm). The resulting van der Waals heterostructure was patterned using electron beam lithography to define contact regions. Reactive ion etching was then used to selectively remove the areas unprotected by a lithographic mask, resulting in trenches for depositing electrical leads. Metal contacts to BLG were made by evaporating 3 nm of chromium and 60 nm of gold. Afterwards, a second round of e-beam lithography was used to design the top gate. The graphene channel was finally defined by a third round of e-beam lithography, followed by reactive ion etching using Poly(methyl methacrylate) and gold top gate as the etching mask. Finally, a fourth round of e-beam lithography was used to pattern large bow-tie antenna connected to the source and the top-gate terminals, followed by evaporation of 3 nm of Cr and 400 nm of Au. Antennas were designed to operate at an experimentally relevant frequency range.

Responsivity measurements. To perform the photoresponse measurements we used variable temperature optical cryostat equipped with a polyethylene window that allowed us to couple the photodetector to incident THz radiation. A Zytech-106 infrared filter was mounted in the radiation shield of the cryostat to block the 300 K background radiation. The radiation was focused to the bow-tie antenna by a silicon hemispherical lens attached to the silicon side of the chip. The transparency of the silicon wafers to the incident THz radiation over the entire T -range was verified by transmission measurements using a THz spectrometer. Photovoltage was recorded using a home-made data acquisition system based on the PXI-e 6363 DAQ board.

The responsivity of our tunneling-enabled detector was calculated assuming that the full power delivered to the device antenna funnelled into the FET channel. The R_v determined by this way provides a lower bound for the detectors' responsivity and is usually referred to as extrinsic. The calculation procedure comprised several steps. First the drain-to-source voltage was recorded as a function of the top gate voltage in the dark (V_{dark}). Then, the dependence of the drain-to-source voltage, V_{DS} , on V_{tg} was obtained under the illumination with THz radiation. The latter was provided by a calibrated backward wave oscillator generating ≈ 0.13 THz radiation with the output power $P_{\text{out}} \approx 1$ mW accurately measured using Golay cell. To ensure the characterization of the detector in the linear-response regime, P_{out} was further attenuated down to $P_{\text{full}} \approx 2$ μW , being the full power delivered to the cryostat window. The difference $V_{\text{ph}} = V_{\text{DS}} - V_{\text{dark}}$ formed the photovoltage. The responsivity was then calculated as $R_v = V_{\text{ph}}/P_{\text{in}}$, where $P_{\text{in}} \approx P_{\text{full}}/3.5$ is the power delivered to the antenna after taking into account the losses in the

silicon lens and the cryostat optical window (≈ 5.5 dB).

In order to study the photoresponse of our detectors at higher f , we used a quantum cascade continuous wave laser based on a GaAs/Al_{0.1}Ga_{0.9}As heterostructure emitting $f = 2.026$ THz radiation. Due to the low power of the QCL and non-optimized antenna design at this f , the calibration of the delivered to the device antenna power was rather challenging and therefore we only report tunneling-enabled operation of our detector in relative units.

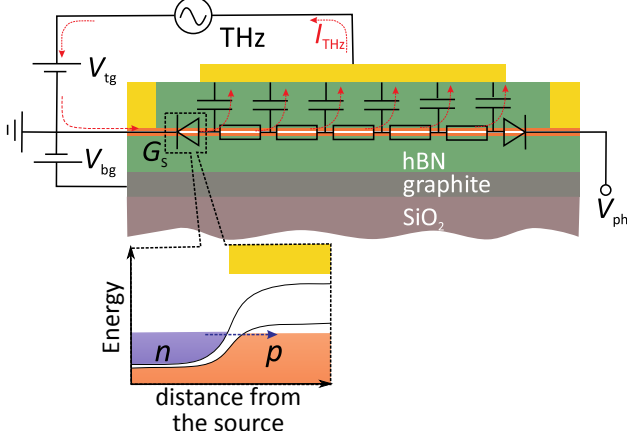


Fig. 5 Equivalent circuit of the BLG TFET detector. Antenna is modelled as an equivalent voltage source V_{ant} that generates ac current I_{THz} (red arrows) flowing into the source and escaping the FET channel through the gate capacitance. Rectification occurs mainly at the tunnel barrier between source and channel (see band alignment profile in the inset) with voltage-dependent conductance G_S . The doping level and the band gap size is controlled via a simultaneous action of the top and bottom gate voltages, V_{tg} and V_{bg} respectively. The photovoltage, V_{ph} , is read out between the source and drain terminals.

Rectification modelling. Our detector can be modelled by an equivalent circuit (shown in Fig. 5) comprising an effective voltage source V_{ant} mimicking an antenna and two nonlinear junctions connected in series with transistor channel. The detector asymmetry, required to obtain a finite photovoltage at zero bias, is provided by the asymmetric connection of antenna between source and gate, and by zero-current condition at the drain. Calculation of detector voltage responsivity $R_v = V_{\text{ph}}/P_{\text{in}}$ includes three distinct steps:

1. Relating the non-linear $I(V)$ characteristics of circuit elements to the rectified voltage V_{ph} .
2. Relating the power incident on antenna with its open-circuit voltage V_{ant} .
3. Microscopic calculation of $I(V)$ characteristics for BLG channel and its tunnel contacts.

First, it is convenient to introduce “voltage-voltage” responsivity of the TFET, $R_{\text{TFET}} = V_{\text{out}}/V_{\text{ant}}^2$. The responsivity of bare transistor channel coupled to antenna between source and drain is the log-derivative of the dc channel conductance G_{ch} with respect to the top gate voltage V_{tg} ²¹, up to a geometrical factor:

$$R_{\text{ch},i} = -\frac{1}{2} \frac{d_b}{d_t + d_b} \frac{\partial \ln G_{\text{C,dc}}}{\partial V_{\text{tg}}}. \quad (2)$$

The presence of a tunnel junction with conductance G_S (assumed frequency-independent) depending on the voltage at the junction V_{TJ} and the top gate voltage V_{tg} results in two extra contributions to R_{TFET} , which also take the form of log-derivatives:

$$R_{\text{TJ},i} = -\frac{1}{2} \frac{\partial \ln G_S}{\partial V_{\text{TJ}}}, \quad R_{\text{TG},i} = -\frac{\partial \ln G_S}{\partial V_{\text{tg}}}. \quad (3)$$

Summation law (1) for individual responsivities (2) and (3) follows directly from Kirchhoff’s circuit rules.

At the second stage, the experimentally measured “voltage-power” responsivity of the photodetector R_v is related to the “voltage-voltage” responsivity of the TFET as

$$R_v = 4Z_{\text{rad}} \left| \frac{Z_{\text{GS}}}{Z_{\text{GS}} + Z_{\text{rad}}} \right|^2 R_{\text{TFET}}, \quad (4)$$

assuming the incident radiation is focused within the antenna’s effective aperture. The prefactor describes voltage division between the TFET impedance Z_{GS} between gate and source and antenna radiation resistance Z_{rad} .

Finally, we calculate the $I(V_d, V_{\text{tg}})$ -characteristics of circuit elements microscopically. The FET channel is described within drift-diffusive model with constant mobility $\mu_{\text{BLG}} = 10^5 \text{ cm}^2/(\text{V}\cdot\text{s})$, a value close to that found in the experiment. Short junctions are described within quantum ballistic model⁵⁴. Both the flux of carriers incident on tunnel barrier and its transparency depend on BLG band structure. This model results in an approximate relation for source junction conductance $G_S \approx \frac{2e}{\pi^{3/2}\hbar} \mathcal{D}_{\text{tun}} k_{\perp\text{tun}} W$, where \mathcal{D}_{tun} is the barrier transparency for normal incidence, and $k_{\perp\text{tun}}$ is the characteristic transverse momentum of electrons participating in tunneling. To obtain vanishing junction resistance in the absence of tunnel barrier, \mathcal{D}_{tun} was replaced by $\mathcal{D}_{\text{tun}}/(1 - \mathcal{D}_{\text{tun}})$ ⁶³. The appearance of high-transparency regions across the tunnel barrier due to local electric potential fluctuations was modelled as an increase of the average field inside the tunnel barrier F_{tun} by a constant value F_{fluct} . A value of $F_{\text{fluct}} \approx 8 \text{ kV/cm}$ was extracted from the experimental resistance $R_{2\text{pt}}$ in the tunneling regime of detector operation.

The calculation of TFET band structure in the double-gated and single-gated regions is based on a parallel-plate capacitor model supplemented with relations between charge densities on graphene layers, their electric potentials, and BLG bandstructure⁶⁴. The transient region with tunnel junction was modelled using an original approach, where screening by the charges in BLG was treated approximately by placing a fictitious conducting plane under BLG. The position and potential of this plane are chosen to yield the correct electric potential deep inside the source and channel regions of the BLG. This reduces our electrostatic problem to finding the fringing field of a capacitor, solved analytically by Maxwell⁶⁵.

ACKNOWLEDGEMENTS

This work was supported by the Russian Foundation for Basic Research within Grants No. 18-37-20058 and No. 18-29-20116. Experimental work of IG (photoresponse measurements) was supported by the Russian Foundation for Basic Research (grant 19-32-80028). We acknowledge support of the Russian Science Foundation grant No. 19-72-10156 (NEP analyses) and grant No. 17-72-30036 (transport measurements). The work of GA and DS (theory of THz detection) was supported by grant # 16-19-10557 of the Russian Scientific Foundation. K.W. and T.T. acknowledge support from the Elemental Strategy Initiative conducted by the MEXT, Japan, Grant Number JPMXP0112101001, JSPS KAKENHI Grant Number JP20H00354 and the CREST(JPMJCR15F3), JST. D.A.B. acknowledges financial support from Leverhulme Trust. The authors thank A. Laisukas, W. Knap, A. I. Berdyugin, Q. Ma and M.S. Shur for helpful discussions.

DATA AVAILABILITY

All data supporting this study and its findings are available within the article and its Supplementary Information or from the corresponding authors upon reasonable request.

AUTHOR CONTRIBUTIONS

D.S. and D.A.B. conceived the experiment. S.G.X. fabricated devices designed by D.A.B. Photoresponse measurements were carried out by I.G., M.M., and D.A.B. Data analysis was performed by I.G., D.A.B. and D.S. Theory analysis was done by G.A. and D.S. The manuscript was written by D.A.B., G.A. and D.S. with input from I.G. and G.F. Experimental support was provided by I.T., M.M., G.G. and A.K.G.; T.T. and K.W. grew the hBN crystals. D.S., G.F. and D.A.B supervised the project. All authors contributed to discussions.

COMPETING INTERESTS

The authors declare no competing interests.

REFERENCES

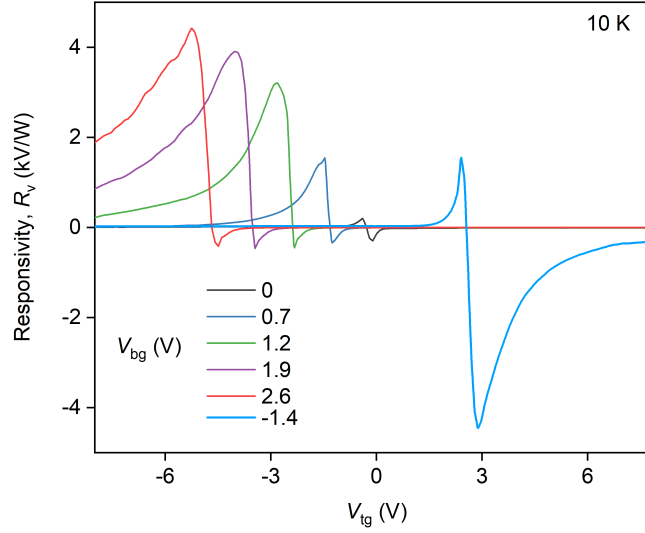
1. Dyakonov, M. & Shur, M. [Detection, mixing, and frequency multiplication of terahertz radiation by two-dimensional electronic fluid.](#) *IEEE Trans. El. Dev.* **43**, 380–387 (1996).
2. Knap, W. *et al.* [Field effect transistors for terahertz detection: Physics and first imaging applications.](#) *Journal of Infrared, Millimeter, and Terahertz Waves* **30**, 1319–1337 (2009).
3. Boppel, S. *et al.* [CMOS integrated antenna-coupled field-effect transistors for the detection of radiation from 0.2 to 4.3 THz.](#) *IEEE Transactions on Microwave Theory and Techniques* **60**, 3834–3843 (2012).
4. Hou, H., Liu, Z., Teng, J., Palacios, T. & Chua, S. [High temperature terahertz detectors realized by a GaN high electron mobility transistor.](#) *Scientific reports* **7**, 46664 (2017).
5. Viti, L. *et al.* [Thermoelectric graphene photodetectors with subnanosecond response times at terahertz frequencies.](#) *Nanophotonics* **1** (2020).
6. Muravev, V. M., Solov'ev, V. V., Fortunatov, A. A., Tsydynzhapov, G. & Kukushkin, I. V. [On the response time of plasmonic terahertz detectors.](#) *JETP Letters* **103**, 792–794 (2016).
7. Rumyantsev, S., Liu, X., Kachorovskii, V. & Shur, M. [Homodyne phase sensitive terahertz spectrometer.](#) *Applied Physics Letters* **111**, 121105 (2017).
8. Glaab, D. *et al.* [Terahertz heterodyne detection with silicon field-effect transistors.](#) *Applied Physics Letters* **96**, 042106 (2010).
9. Vitiello, M. S. *et al.* [Room-temperature terahertz detectors based on semiconductor nanowire field-effect transistors.](#) *Nano Lett.* **12**, 96–101 (2012).
10. Vicarelli, L. *et al.* [Graphene field-effect transistors as room-temperature terahertz detectors.](#) *Nat. Mater.* **11**, 865–871 (2012).
11. Viti, L. *et al.* [Black phosphorus terahertz photodetectors.](#) *Adv. Mater.* **27**, 5567–5572 (2015).
12. Isobe, H., Xu, S.-Y. & Fu, L. [High-frequency rectification via chiral Bloch electrons.](#) *Science Advances* **6**, eaay2497 (2020).
13. Olbrich, P. *et al.* [Terahertz ratchet effects in graphene with a lateral superlattice.](#) *Phys. Rev. B* **93**, 075422 (2016).
14. Walsh, E. D. *et al.* [Graphene-based Josephson-junction single-photon detector.](#) *Phys. Rev. Applied* **8**, 024022 (2017).
15. Auton, G. *et al.* [Terahertz detection and imaging using graphene ballistic rectifiers.](#) *Nano Lett.* **17**, 7015–7020 (2017).
16. Principi, A., Bandurin, D., Rostami, H. & Polini, M. [Pseudo-Euler equations from nonlinear optics: Plasmon-assisted photodetection beyond hydrodynamics.](#) *Phys. Rev. B* **99**, 075410 (2019).
17. Castilla, S. *et al.* [Fast and sensitive terahertz detection using an antenna-integrated graphene \$p\$ - \$n\$ junction.](#) *Nano Lett.* **19**, 2765–2773 (2019).
18. Muravev, V. M. & Kukushkin, I. V. [Plasmonic detector/spectrometer of subterahertz radiation based on two-dimensional electron system with embedded defect.](#) *Appl. Phys. Lett.* **100**, 082102 (2012).
19. Bandurin, D. A. *et al.* [Resonant terahertz detection using graphene plasmons.](#) *Nat. Commun.* **9**, 5392 (2018).
20. Khavronin, M., Petrov, A., Kazantsev, A., Nikulin, E. & Bandurin, D. [Singularity-enhanced terahertz detection in high-mobility field-effect transistors.](#) *Phys. Rev. Applied* **13**, 064072 (2020).
21. Sakowicz, M. *et al.* [Terahertz responsivity of field effect transistors versus their static channel conductivity and loading effects.](#) *J. Appl. Phys.* **110**, 054512 (2011).
22. Ionescu, A. M. & Riel, H. [Tunnel field-effect transistors as energy-efficient electronic switches.](#) *Nature* **479**, 329–337 (2011).
23. Sarkar, D. *et al.* [A subthermionic tunnel field-effect transistor with an atomically thin channel.](#) *Nature* **526**, 91–95 (2015).
24. Lu, H. & Seabaugh, A. [Tunnel field-effect transistors: State-of-the-art.](#) *IEEE J. El. Dev. Soc.* **2**, 44–49 (2014).
25. Emboras, A. *et al.* [Atomic scale plasmonic switch.](#) *Nano Lett.* **16**, 709–714 (2016).
26. Baski, A., Albrecht, T. & Quat, C. [Tunnelling accelerometer.](#) *Journal of Microscopy* **152**, 73–76 (1988).
27. Sarkar, D., Gossner, H., Hansch, W. & Banerjee, K. [Tunnel-field-effect-transistor based gas-sensor: Introducing gas detection with a quantum-mechanical transducer.](#) *Appl. Phys. Lett.* **102**, 023110 (2013).
28. Sarkar, D. & Banerjee, K. [Proposal for tunnel-field-effect-transistor as ultra-sensitive and label-free biosensors.](#) *Appl. Phys. Lett.* **100**, 143108 (2012).
29. Gao, A., Lu, N., Wang, Y. & Li, T. [Robust ultrasensitive tunneling-FET biosensor for point-of-care diagnostics.](#) *Sci. Rep.* **6**, 22554 (2016).
30. Yang, Q. *et al.* [Performance evaluation of tunneling field effect transistor on terahertz detection.](#) *2018 China Semiconductor Technology International Conference (CSTIC)* 1–3 (2018).
31. Okamoto, T., Fujimura, N., Crespi, L., Kodera, T. & Kawano, Y. [Terahertz detection with an antenna-coupled highly-doped silicon quantum dot.](#) *Sci. Rep.* **9**, 18574 (2019).
32. Rinzan, M., Jenkins, G., Drew, H. D., Shafranjuk, S. & Barbara, P. [Carbon nanotube quantum dots as highly sensitive terahertz-cooled spectrometers.](#) *Nano Lett.* **12**, 3097–3100 (2012).
33. Liu, L., Rahman, S. M., Jiang, Z., Li, W. & Fay, P. [Advanced terahertz sensing and imaging systems based on integrated III-V interband tunneling devices.](#) *Proc. IEEE* **105**, 1020–1034 (2017).
34. Kang, T. *et al.* [Terahertz rectification in ring-shaped quantum barriers.](#) *Nat. Commun.* **9**, 4914 (2018).
35. Nishida, Y. *et al.* [Terahertz coherent receiver using a single resonant tunnelling diode.](#) *Sci. Rep.* **9**, 18125 (2019).
36. Sharma, A., Singh, V., Bougher, T. L. & Cola, B. A. [A carbon nanotube optical rectenna.](#) *Nat. Nanotechnol.* **10**, 1027–1032 (2015).
37. Davids, P. S. *et al.* [Infrared rectification in a nanoantenna-coupled metal-oxide-semiconductor tunnel diode.](#) *Nat. Nanotechnol.* **10**, 1033–1038 (2015).
38. Ward, D. R., Hüser, F., Pauly, F., Cuevas, J. C. & Natelson, D. [Optical rectification and field enhancement in a plasmonic nanogap.](#) *Nat. Nanotechnol.* **5**, 732–736 (2010).
39. Ariyoshi, S. *et al.* [Terahertz imaging with a direct detector based on superconducting tunnel junctions.](#) *Appl. Phys. Lett.* **88**, 203503 (2006).
40. Vischi, F. *et al.* [Electron cooling with graphene-insulator-superconductor tunnel junctions for applications in fast bolometry.](#) *Phys. Rev. Applied* **13**, 054006 (2020).
41. Lee, G.-H. *et al.* [Graphene-based Josephson junction microwave bolometer.](#) *Nature* **586**, 42–46 (2020).
42. Chakraborty, A. & Sarkar, A. [Investigation of analog/RF performance of staggered heterojunctions based nanowire tunneling field-effect transistors.](#) *Superlattices and Microstructures* **80**, 125 – 135 (2015).

43. Ryzhii, V. & Shur, M. S. Resonant terahertz detector utilizing plasma oscillations in two-dimensional electron system with lateral Schottky junction. *Jpn. J. Appl. Phys.* **45**, L1118–L1120 (2006).
44. McCann, E. & Fal’ko, V. I. Landau-level degeneracy and quantum Hall effect in a graphite bilayer. *Phys. Rev. Lett.* **96**, 086805 (2006).
45. Zhang, Y. *et al.* Direct observation of a widely tunable bandgap in bilayer graphene. *Nature* **459**, 820–823 (2009).
46. Banszerus, L. *et al.* Gate-defined electron–hole double dots in bilayer graphene. *Nano Lett.* **18**, 4785–4790 (2018).
47. Eich, M. *et al.* Coupled quantum dots in bilayer graphene. *Nano Lett.* **18**, 5042–5048 (2018).
48. Eich, M. *et al.* Spin and valley states in gate-defined bilayer graphene quantum dots. *Phys. Rev. X* **8**, 031023 (2018).
49. Kretinin, A. V. *et al.* Electronic properties of graphene encapsulated with different two-dimensional atomic crystals. *Nano Lett.* **14**, 3270–3276 (2014).
50. Zibrov, A. A. *et al.* Tunable interacting composite fermion phases in a half-filled bilayer-graphene Landau level. *Nature* **549**, 360–364 (2017).
51. Spirito, D. *et al.* High performance bilayer-graphene terahertz detectors. *Appl. Phys. Lett.* **104**, 061111 (2014).
52. Bandurin, D. A. *et al.* Dual origin of room temperature sub-terahertz photoresponse in graphene field effect transistors. *Appl. Phys. Lett.* **112**, 141101 (2018).
53. Raikh, M. & Ruzin, I. Transparency fluctuations in randomly inhomogeneous barriers of finite area. *Sov. Phys. JETP* **65**, 1273–1282 (1987).
54. Alymov, G., Vyurkov, V., Ryzhii, V. & Svintsov, D. Abrupt current switching in graphene bilayer tunnel transistors enabled by van Hove singularities. *Sci. Rep.* **6**, 24654 (2016).
55. Petrosyan, S. & Shik, A. Y. Contact phenomena in low-dimensional electron systems. *Zh. Eksp. Teor. Fiz* **69**, 1261 (1989).
56. Smith, A. D., Tinkham, M. & Skocpol, W. J. New thermoelectric effect in tunnel junctions. *Phys. Rev. B* **22**, 4346–4354 (1980).
57. Bauer, M. *et al.* A high-sensitivity AlGaIn/GaN HEMT terahertz detector with integrated broadband bow-tie antenna. *IEEE Transactions on Terahertz Science and Technology* **9**, 430–444 (2019).
58. Sanchez, A., Davis Jr, C. F., Liu, K. C. & Javan, A. The MOM tunneling diode: Theoretical estimate of its performance at microwave and infrared frequencies. *Journal of Applied Physics* **49**, 5270–5277 (1978).
59. Kim, S. *et al.* Thickness-controlled black phosphorus tunnel field-effect transistor for low-power switches. *Nat. Nanotechnol.* **15**, 203–206 (2020).
60. Gandhi, R., Chen, Z., Singh, N., Banerjee, K. & Lee, S. Vertical Si-nanowire *n*-type tunneling FETs with low subthreshold swing (≤ 50 mV/decade) at room temperature. *IEEE Electron Device Letters* **32**, 437–439 (2011).
61. Shukla, N. *et al.* A steep-slope transistor based on abrupt electronic phase transition. *Nature communications* **6**, 1–6 (2015).
62. Si, M. *et al.* Steep-slope hysteresis-free negative capacitance MoS₂ transistors. *Nature nanotechnology* **13**, 24–28 (2018).
63. Datta, S. *Electronic Transport in Mesoscopic Systems* (Cambridge university press, 1997).
64. Castro, E. V. *et al.* Electronic properties of a biased graphene bilayer. *Journal of Physics: Condensed Matter* **22**, 175503 (2010).
65. Maxwell, J. C. *A Treatise on Electricity and Magnetism*, vol. 1 (Clarendon press, 1873). Art. 202.

Supporting information

SUPPLEMENTARY NOTE 1: FURTHER EXAMPLES OF TUNNEL-ENABLED PHOTORESPONSE

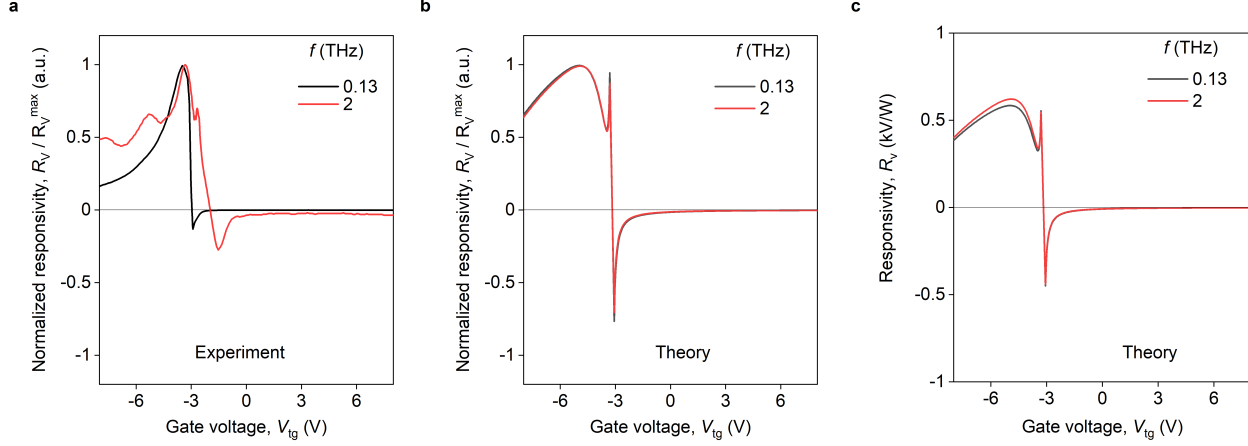
Supplementary Figure 1 shows further examples of our tunnel detector responsivity R_v as a function of V_{tg} recorded in response to $f = 0.13$ THz radiation for varying V_{bg} . For all $V_{bg} \neq 0$, $R_v(V_{tg})$ dependencies are highly asymmetric. With increasing V_{bg} , R_v is increasing and for $V_{bg} = 2.6$ V reaches 4.5 kV/W overcoming zero V_{bg} value by more than an order of magnitude. A similar behaviour was observed if the polarity of V_{bg} is reversed (blue curve in Supplementary Figure 1). These observations highlights a drastic difference between the field-effect-enabled intraband (black curve) rectification and its interband tunneling counterpart (all other curves).



Supplementary Fig. 1 Tunneling-enabled THz detection. R_v as a function of V_{tg} for given V_{bg} recorded in response to 0.13 THz radiation. $T = 10$ K.

SUPPLEMENTARY NOTE 2: FREQUENCY DEPENDENCE OF TUNNELLING-ENABLED PHOTORESPONSE

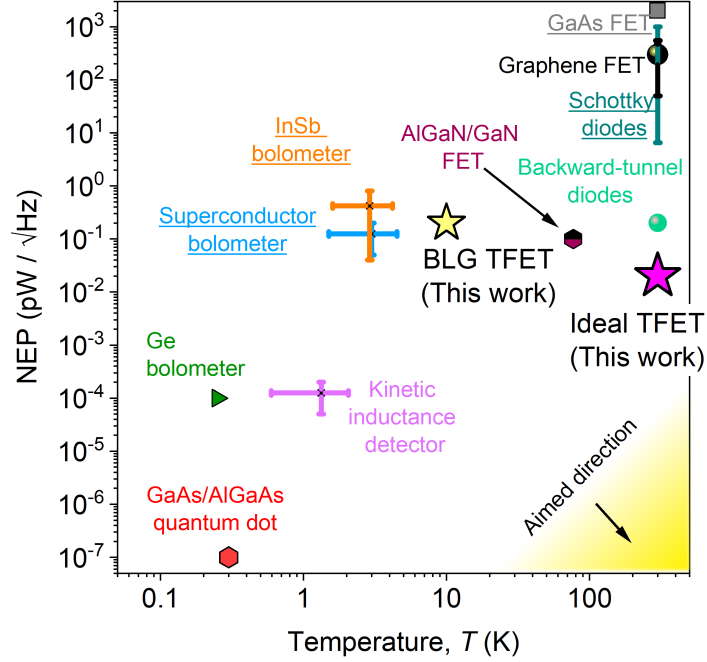
We have also studied the response of our detectors at higher frequency and found consistent tunnelling-enabled highly-asymmetric behaviour when the top and bottom gates are biased with opposite polarity. Examples of $R_v(V_{tg})$ are shown in Supplementary Figure 2a for two characteristic f from sub-THz and THz domains. Note, due to the limitation of our measurements (see [Methods](#)) we only present a relative comparison between $R_v(V_{tg})$ recorded at $f = 0.13$ THz and $f = 2$ THz. However, our modelling which provides remarkable agreement with experiment at $f = 0.13$ THz predicts that TFET detectors are expected to perform equivalently well at both sub-THz and THz frequencies as we show in Supplementary Figures 2b,c.



Supplementary Fig. 2 Frequency dependence of tunnelling-assisted THz detection. **a** R_v as a function of V_{tg} for $V_{bg} = 1.2$ V obtained under illumination with THz radiation of given frequency. The data normalized to their maximum value. Peaks in R_v correspond to the excitation of plasmon-resonances in the detector channel^{S1}. **b, c** Theoretical $R_v(V_{tg})$ dependencies for given f : as-calculated (**c**) and normalized to their maximum value (**b**).

SUPPLEMENTARY NOTE 3: COMPARISON WITH EXISTING TECHNOLOGY

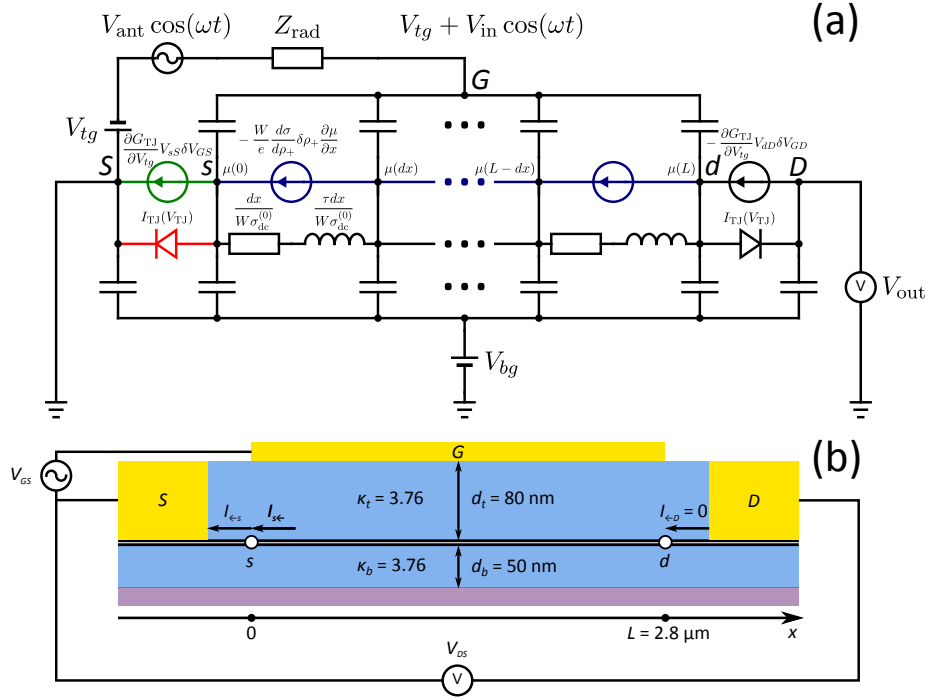
In Supplementary Figure 3 we compare the performance of our tunnel device with other THz detectors and rectifiers; some of them are available on the market (underlined labels). To this end, we plot their noise equivalent power (NEP) versus temperature, T , at which they operate. The comparison is made for the frequency range 0.1 – 2 THz and for the NEP calculated via extrinsic responsivity, i.e. which takes into account the full power delivered to the device. The devices of different types are compared: cooled superconducting bolometers^{S2,S3}, cooled semiconducting bolometers^{S4–S6}, kinetic inductance sensors^{S7,S8}, cooled quantum dot devices^{S9,S10}, as well as transistor-based detectors^{S1,S11–S18}, Schottky diodes^{S19–S21}, and heterostructure backward diodes^{S22,S23}. One of the primary tasks for the next-generation THz technology is to produce low-NEP sensors operating at elevated temperatures as indicated by the yellow shaded area in Supplementary Figure 3. However, whereas the cooled devices feature exceptionally low NEP, room- T devices are usually characterized by much higher NEP. Our BLG TFET offers a compromise to this enquiry: it features relatively low NEP and operates above liquid helium T . Furthermore, our model suggests that TFETs with optimized parameters can feature even lower NEP at room temperature (magenta star in Supplementary Figure 3) and thus offer a route to the next-generation THz technology. The details are given in [Supplementary Note 5](#).



Supplementary Fig. 3 Overview of THz detectors. NEP for THz detectors of various types plotted against the temperature at which they operate. Vertical error bars represent the spread of the detectors' performance over the frequency range 0.1 – 2 THz. Horizontal error bars show the temperature range at which the detectors operate. Underlined labels denote commercial technology.

SUPPLEMENTARY NOTE 4: THEORETICAL MODEL OF A BLG TFET PHOTODETECTOR

SUPPLEMENTARY NOTE 4.1: MODELLING OF TUNNELING-ASSISTED THZ DETECTION



Supplementary Fig. 4 Equivalent circuit. **a**, Detailed equivalent circuit of a TFET-based detector. Different colors show the origins of different contributions to responsivity: nonlinear current-voltage characteristic of the tunnel junction between source and channel (red), its gate-controlled conductance (represented as an equivalent current source, green), and the gate-controlled channel conductance (represented as a distributed current source, blue). **b**, Schematic view of our photodetector showing some of the notation used throughout the Supplementary Information.

In this section, we derive a general expression for the responsivity of a TFET. The relevant circuit is shown in Supplementary Figure 4a. We will treat the TFET as if it was single-gated, since the bottom gate is held at a constant potential and its only function is to open a bandgap in BLG.

A TFET consists of two rectification units: a tunnel junction between the source and the channel, and the channel itself. (The drain tunnel junction is effectively excluded from the circuit by the zero drain current assumption, at least if the junction is too short to accommodate any spatial inhomogeneities of the current.)

When a small ac voltage $V_{in} \cos(\omega t)$ is applied between the gate and source, it induces voltages and currents in different parts of the detector, having the general form $(\delta V, \delta I)(t) = \text{Re} \left[(V, I)^{(1)} e^{-i\omega t} \right] + (V, I)^{(2)} + \dots \cdot e^{\pm 2i\omega t} + o(V_{in}^2)$, where we are interested in the first-order and dc second-order components.

We use a non-distributed model for the source junction, meaning current can flow through the junction only in presence of a nonzero voltage drop across the junction and not solely under the action of ac gate voltage. Keeping this in mind, the second-order expansion of its current-voltage characteristic $I_{\leftarrow s}(V_{ss}, V_{GS})$ reads

$$\begin{aligned} I_{\leftarrow s}^{(1)} &= G_S(\omega) V_{ss}^{(1)}, \\ I_{\leftarrow s}^{(2)} &= G_{S,dc} \left[V_{ss}^{(2)} - R_{TJ,i} \frac{|V_{ss}^{(1)}|^2}{2} - R_{TG,i} \frac{\text{Re} \left(V_{GS}^{(1)} V_{ss}^{(1)*} \right)}{2} \right], \end{aligned} \quad (\text{S1})$$

where $G_{S,dc}$ and $G_S(\omega)$ are the dc and ac conductance of the junction, $R_{TJ,i}$ is the intrinsic tunnel junction responsivity, and $R_{TG,i}$ is the intrinsic “tunnel-gate” responsivity.

When writing similar expressions for the current $I_{s\leftarrow}$ flowing to the source from the channel, we make advantage of the linear dependence between $V_{ds}^{(1)}$ and $V_{Gs}^{(1)}$ arising from zero drain current condition, and use only $V_{Gs}^{(1)}$ and $V_{ds}^{(2)}$ as independent variables (remember that dc gate voltage $V_{Gs}^{(2)}$ does not produce any current by itself):

$$\begin{aligned} I_{s\leftarrow}^{(1)} &= \tilde{G}_{ch}(\omega) V_{Gs}^{(1)}, \\ I_{s\leftarrow}^{(2)} &= G_{ch,dc} \left[V_{ds}^{(2)} - R_{ch,i} \frac{|V_{Gs}^{(1)}|^2}{2} \right], \end{aligned} \quad (\text{S2})$$

where $G_{ch,dc}$ is the dc channel conductance, $\tilde{G}_{ch}(\omega) \equiv (\partial I_{s\leftarrow}(\omega) / \partial V_{Gs}(\omega))|_{I_{\leftarrow d}=0}$ is the ac channel conductance measured between source and gate, and $R_{ch,i}$ is the intrinsic channel responsivity.

From continuity of current, $I_{\leftarrow s}^{(1)} = I_{s\leftarrow}^{(1)}$ and $I_{\leftarrow s}^{(2)} = I_{s\leftarrow}^{(2)} = I_{\leftarrow D}^{(2)} = 0$, we find that the ac voltage $V_{GS}^{(1)} \equiv V_{in}$ applied between the gate and source is divided into voltage $V_{sS}^{(1)}$ at the source tunnel junction and voltage $V_{Gs}^{(1)}$ between the gate and the beginning of the channel:

$$\begin{aligned} V_{sS}^{(1)} &= \frac{\tilde{G}_{ch}(\omega)}{G_S(\omega) + \tilde{G}_{ch}(\omega)} V_{in}, \\ V_{Gs}^{(1)} &= \frac{G_S(\omega)}{G_S(\omega) + \tilde{G}_{ch}(\omega)} V_{in}, \end{aligned} \quad (S3)$$

which are subsequently rectified by the tunnel junction and the channel:

$$\begin{aligned} V_{sS}^{(2)} &= R_{TJ,i} \frac{|V_{sS}^{(1)}|^2}{2} + R_{TG,i} \frac{\text{Re}(V_{Gs}^{(1)} V_{sS}^{(1)*})}{2}, \\ V_{ds}^{(2)} &= R_{ch,i} \frac{|V_{Gs}^{(1)}|^2}{2}. \end{aligned} \quad (S4)$$

These rectified voltages sum together to yield the output voltage $V_{DS}^{(2)} \equiv V_{out}$ of the photodetector (remember that the voltage at the drain junction $V_{Dd}^{(2)} = 0$ because of zero drain current). Total responsivity of the TFET is given by the sum of tunnel junction responsivity, coming from the nonlinear current-voltage characteristic of the source tunnel junction, tunnel-gate responsivity, coming from resistive self-mixing in the gate-controlled source tunnel junction, and channel responsivity, coming from resistive self-mixing in the channel:

$$\begin{aligned} R_{TFET} &\equiv \frac{V_{out}}{V_{in}^2/2} \equiv \frac{V_{DS}^{(2)}}{(V_{GS}^{(1)})^2/2} = R_{TJ} + R_{TG} + R_{ch}, \\ R_{TJ} &\equiv \left| \frac{\tilde{G}_{ch}(\omega)}{G_S(\omega) + \tilde{G}_{ch}(\omega)} \right|^2 R_{TJ,i}, \\ R_{TG} &\equiv \text{Re} \frac{\tilde{G}_{ch}(\omega)}{G_S(\omega) + \tilde{G}_{ch}(\omega)} R_{TG,i}, \\ R_{ch} &\equiv \left| \frac{G_S(\omega)}{G_S(\omega) + \tilde{G}_{ch}(\omega)} \right|^2 R_{ch,i}. \end{aligned} \quad (S5)$$

We will neglect the frequency dependence of the tunnel junction current-voltage characteristic. With this assumption, intrinsic tunnel junction and tunnel-gate responsivities are given by the logarithmic derivatives of the junction conductance with respect to appropriate voltages:

$$\begin{aligned} R_{TJ,i} &= -\frac{1}{2} \left(\frac{\partial \ln G_S}{\partial V_{sS}} \right)_{V_{GS}}, \\ R_{TG,i} &= - \left(\frac{\partial \ln G_S}{\partial V_{GS}} \right)_{V_{sS}}. \end{aligned} \quad (S6)$$

Due to the distributed nature of the channel, its current-voltage characteristics are inherently frequency-dependent. Nevertheless, the intrinsic channel responsivity can also be expressed in terms of the logarithmic derivative of its dc conductance, see [Supplementary Note 4.6](#):

$$R_{ch,i} \approx -\frac{1}{2} \frac{d_b}{d_t + d_b} \left(\frac{\partial \ln G_{ch,dc}}{\partial V_{GS}} \right)_{V_{ds}=0}. \quad (S7)$$

A similar expression was originally derived in Ref. [S24](#) for a single-gated FET. The extra prefactor represents the gate voltage division in a double-gated structure with top and bottom gate dielectrics of thicknesses d_t, d_b .

TFET responsivity (S5) describes its response to the ac voltage at the gate, while the experimentally measured photodetector responsivity R_v describes response to the power P_{in} incident on the antenna. The relation between these responsivities can be obtained by considering the complete circuit of the photodetector, including the antenna radiation resistance $Z_{rad}(\omega)$ (Supplementary Figure 4a). Assuming the incident radiation is focused within the antenna's effective aperture, the incident power can be converted into the effective voltage $V_{ant} = \sqrt{8Z_{rad}(\omega)P_{in}}$ ^{S25}, which is divided between $Z_{rad}(\omega)$ and the TFET gate-to-source ac impedance

$$Z_{GS}(\omega) = G_S^{-1} + \tilde{G}_{ch}^{-1}(\omega), \quad (S8)$$

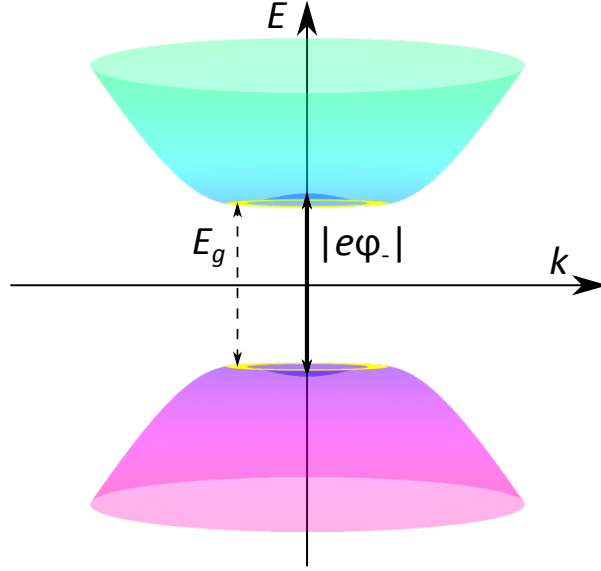
yielding

$$R_v \equiv \frac{V_{out}}{P_{in}} = 8Z_{rad}(\omega) \frac{V_{out}}{|V_{ant}|^2} = 4Z_{rad}(\omega) \left| \frac{Z_{GS}(\omega)}{Z_{GS}(\omega) + Z_{rad}(\omega)} \right|^2 R_{TFET}. \quad (S9)$$

SUPPLEMENTARY NOTE 4.2: BANDSTRUCTURE AND CHARGE DENSITY IN BILAYER GRAPHENE

BLG in external electric field is described by the Hamiltonian^{S26,S27}

$$\hat{H}(\mathbf{k}) = \begin{pmatrix} -e\varphi_t & \hbar v_0(\pm k_x - ik_y) & 0 & 0 \\ \hbar v_0(\pm k_x + ik_y) & -e\varphi_t & \gamma_1 & 0 \\ 0 & \gamma_1 & -e\varphi_b & \hbar v_0(\pm k_x - ik_y) \\ 0 & 0 & \hbar v_0(\pm k_x + ik_y) & -e\varphi_b \end{pmatrix}, \quad (S10)$$



Supplementary Fig. 5 Bilayer graphene bandstructure. Bandstructure of biased bilayer graphene described by Hamiltonian (S10) (only the conduction and valence bands are shown). Circular band extrema are highlighted in yellow.

in the vicinity of K, K' points of the Brillouin zone, where φ_t, φ_b are the electric potentials at top and bottom graphene layers, $\gamma_1 = 0.38$ eV, $v_0 = 10^6$ m/s, and the signs depend on the valley.

The corresponding conduction and valence band dispersions are

$$E_{c,v}(k) = -e\varphi_+ \pm E(k),$$

$$E(k) = \sqrt{\frac{E_g^2}{4} + \left[\sqrt{\frac{\gamma_1^2 - E_g^2}{4} + (\hbar v_0 k)^2} - \frac{\gamma_1^2}{2\sqrt{\gamma_1^2 - E_g^2}} \right]^2} \quad (\text{S11})$$

with a bandgap

$$E_g(\varphi_-) = \frac{\gamma_1}{\sqrt{\gamma_1^2 + e^2\varphi_-^2}} |e\varphi_-|, \quad (\text{S12})$$

where $\varphi_+ \equiv (\varphi_t + \varphi_b)/2$ is the average potential of graphene layers, and $\varphi_- \equiv \varphi_t - \varphi_b$ is the interlayer voltage. The bands have a “Mexican hat” shape with circular extrema around the corners of the Brillouin zone (Supplementary Figure 5).

The inverse dispersion relation is

$$k_{\pm}(E - e\varphi_+) = \frac{1}{\hbar v_0} \sqrt{E^2 + \frac{e^2\varphi_-^2}{4} \pm \sqrt{(\gamma_1^2 + e^2\varphi_-^2) \left(E^2 - \frac{E_g^2}{4} \right)}}. \quad (\text{S13})$$

It is double-valued within the “Mexican hat” region, $E_g/2 < |E| \leq |e\varphi_-|$, while only a single solution k_+ remains above the hat, $|E| > |e\varphi_-|$.

Given the dispersion relation (S11), we can express the charge density $\rho_+ \equiv \rho_t + \rho_b$ in BLG at zero temperature through the chemical potential measured from the midgap, $\tilde{\mu} \equiv \mu + e\varphi_+$, and vice versa:

$$\rho_+(\tilde{\mu}) = \begin{cases} 0 & \text{if } |\tilde{\mu}| < \frac{E_g}{2}, \\ -e \frac{k_F^2}{\pi} \text{sgn } \tilde{\mu}, k_F = k_+(\tilde{\mu}) & \text{if } |\tilde{\mu}| \geq \frac{|e\varphi_-|}{2}, \\ -e \frac{k_{F+}^2 - k_{F-}^2}{\pi} \text{sgn } \tilde{\mu}, k_{F\pm} = k_{\pm}(\tilde{\mu}) & \text{if } \frac{E_g}{2} < |\tilde{\mu}| < \frac{|e\varphi_-|}{2}, \end{cases} \quad (\text{S14})$$

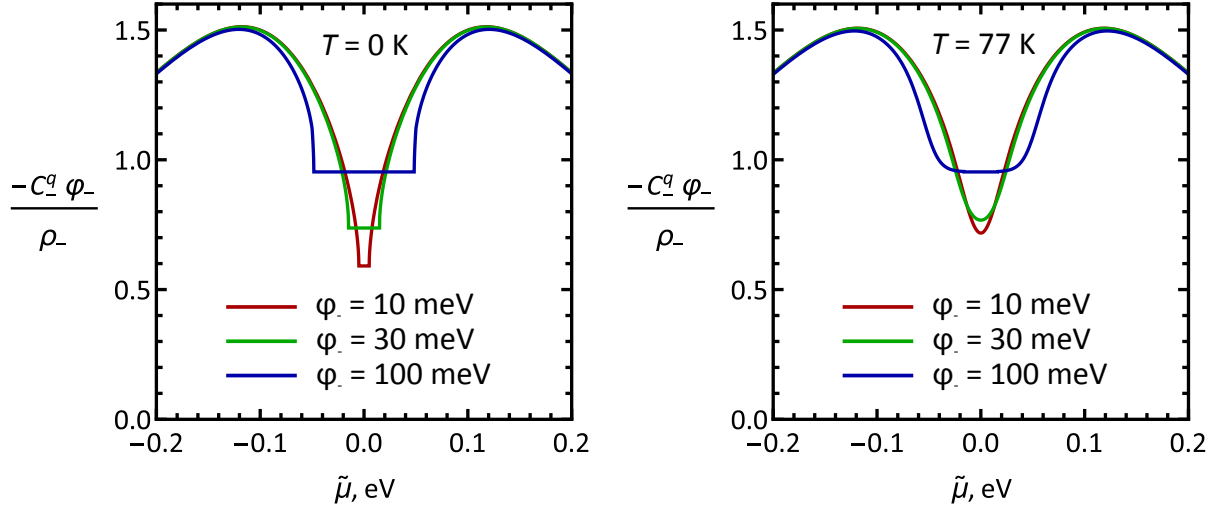
$$\tilde{\mu}(\rho_+) = \begin{cases} -E(k_F) \text{sgn } \rho_+, k_F = \sqrt{\frac{\pi|\rho_+|}{e}} & \text{if } |\rho_+| \geq \rho_{\text{hat}}, \\ -\sqrt{\frac{E_g^2}{4} + \frac{1}{4(\gamma_1^2 + e^2\varphi_-^2)}} \left(\hbar v_0 \sqrt{\frac{\pi|\rho_+|}{e}} \right)^4 \text{sgn } \rho_+ & \text{if } 0 < |\rho_+| < \rho_{\text{hat}} \end{cases}$$

where $\rho_{\text{hat}} = (e/\pi)(e\varphi_-/\hbar v_0)^2$ is the charge density corresponding to $\tilde{\mu} = \pm e\varphi_-/2$ (the Fermi level positioned at the tip of the “Mexican hat”). We have taken into account the double valley degeneracy in BLG.

SUPPLEMENTARY NOTE 4.3: ELECTROSTATICS OF DOUBLE-GATED BILAYER GRAPHENE

To calculate the band diagram of our TFET, we seek approximate analytical solution of electrostatic equations for double-gated BLG.

Let V_{tg}, V_{bg} be the potentials of the top and bottom gate, d_t, d_b the thicknesses of dielectric layers separating BLG from the gates, κ_t, κ_b the dielectric constants of these layers, and d the interlayer distance in BLG. Then, the total charge density $\rho_+ \equiv \rho_t + \rho_b$ and interlayer charge transfer $\rho_- \equiv (\rho_t - \rho_b)/2$ are related to the electric potentials φ_t, φ_b of top and bottom graphene layers by



Supplementary Fig. 6 Accuracy of the constant interlayer quantum capacitance approximation. Ratio between the interlayer charge transfer calculated using a constant interlayer quantum capacitance $C_-^q = 3e^2\gamma_1/(4\pi\hbar^2v_0^2)$ and the exact interlayer charge transfer ρ_- calculated from Hamiltonian (S10) as described in Ref. S26. Left panel: zero temperature, right panel: $T = 77$ K.

$$\begin{aligned}\rho_+ &= -C_t(V_{tg} - \varphi_t) - C_b(V_{bg} - \varphi_b), \\ \rho_- &= -\frac{C_t(V_{tg} - \varphi_t)}{2} + \frac{C_b(V_{bg} - \varphi_b)}{2} + C_-^{\text{cl}}(\varphi_t - \varphi_b),\end{aligned}\quad (\text{S15})$$

where we introduced capacitances per unit area $C_-^{\text{cl}} \equiv \epsilon_0/d$, $C_t \equiv \kappa_t\epsilon_0/d_t$, $C_b \equiv \kappa_b\epsilon_0/d_b$.

The potentials of graphene layers stay close to the Fermi level (compared to the gate voltages), and we can substitute $V_{t/b} - \varphi_{t/b} \rightarrow V_{t/b} + \mu/e$ in the second equation. We cannot do the same in the first equation, otherwise it would not work properly in the undoped case. Instead, in the first equation we approximate $\varphi_t \approx \varphi_b \approx \varphi_+$ to decouple ρ_+ , φ_+ and ρ_- :

$$\begin{aligned}\rho_+ &\approx -C_tV_{tg} - C_bV_{bg} + (C_t + C_b)\varphi_+, \\ \rho_- &= -\frac{C_t(V_{tg} + \mu/e)}{2} + \frac{C_b(V_{bg} + \mu/e)}{2} + C_-^{\text{cl}}\varphi_-.\end{aligned}\quad (\text{S16})$$

The introduced approximations essentially amount to a minor shift of gate voltages, by the order of magnitude equal to φ_t , φ_b .

These equations have to be supplemented with explicit expressions for $\rho_{\pm}(\tilde{\mu}, \varphi_-)$ in BLG ($\tilde{\mu} \equiv \mu + e\varphi_+$ is the chemical potential with respect to the midgap). To facilitate analytical treatment, we use zero-temperature expression for the total charge density (S14) and a constant quantum capacitance model for the interlayer charge transfer:

$$\begin{aligned}\rho_+ &= \begin{cases} 0 & \text{if } |\tilde{\mu}| \leq \frac{E_g(\varphi_-)}{2}, \\ \rho_+(\tilde{\mu}) & \text{if } |\tilde{\mu}| > \frac{E_g(\varphi_-)}{2}, \end{cases} \\ \rho_- &\approx -C_-^q\varphi_-.\end{aligned}\quad (\text{S17})$$

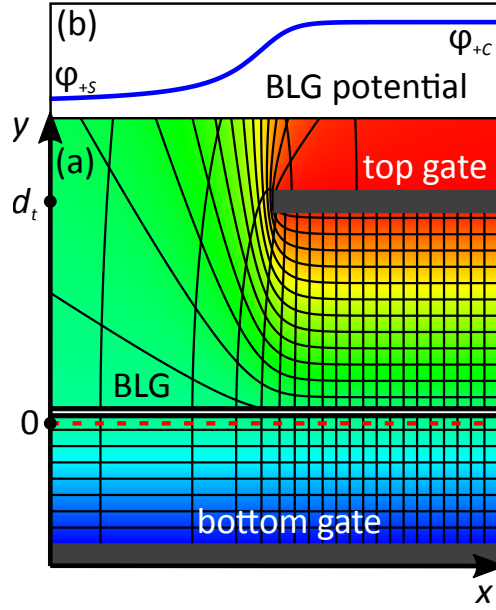
The constant interlayer quantum capacitance $C_-^q = 3e^2\gamma_1/(4\pi\hbar^2v_0^2)$ approximates the interlayer charge transfer in BLG over a wide range of bangaps and doping levels within 50% accuracy (see Supplementary Figure 6).

Now, the equation for ρ_- becomes trivial to solve, while the equation for ρ_+ requires some additional simplifications to allow analytical solution. We consider two opposite cases: (1) Fermi level lies within the bandgap, (2) Fermi level lies outside the gap. In the first case, $\rho_+ = 0$ at zero temperature, and φ_+ is readily obtained from (S16). In the second case, we can pick some initial guess for φ_+ , find ρ_+ from (S16), and find a better approximation for φ_+ from (S17). Since the quantum capacitance $C_+^q \sim \epsilon_0/d$ is much larger than $C_t + C_b$, the precise value of the initial guess is unimportant, and we initially assume the Fermi level is pinned at the band edge, $\tilde{\mu} = \pm E_g/2$ (this choice avoids spurious discontinuities in $\varphi_+(V_{tg}, V_{bg})$).

The overall procedure is summarized in the following equations:

$$\begin{aligned}\varphi_- &\approx \frac{C_t(V_{tg} + \mu/e) - C_b(V_{bg} + \mu/e)}{2C_-}, \quad C_- \equiv C_-^{\text{cl}} + C_-^q, \\ E_g &= E_g(\varphi_-), \\ \tilde{\mu}_0 &= e \frac{C_t(V_{tg} + \mu/e) + C_b(V_{bg} + \mu/e)}{C_t + C_b}, \\ \tilde{\mu} &\approx \begin{cases} \tilde{\mu}_0 & \text{if } |\tilde{\mu}_0| \leq \frac{E_g}{2}, \\ \tilde{\mu}(\rho_+), \rho_+ = -\frac{C_t + C_b}{e} \left(\tilde{\mu}_0 - \frac{E_g}{2} \text{sgn } \tilde{\mu}_0 \right) & \text{if } |\tilde{\mu}_0| > \frac{E_g}{2}, \end{cases}\end{aligned}\quad (\text{S18})$$

where $E_g(\varphi_-)$, $\tilde{\mu}(\rho_+)$ are given by (S12) and (S14).



Supplementary Fig. 7 Electric field in the tunnel junction. **a** Color map showing the distribution of electric potential near the source-channel junction. Black lines: equipotential lines and field lines. Dashed red line: fictitious conductor introduced to obtain the correct potential in the source and the channel without explicitly considering screening by BLG. Potential above the fictitious conductor was calculated as prescribed in Ref. S29, potential below the fictitious conductor was calculated in the parallel-plate capacitor model. **b** Electric potential $\varphi_+(x)$ inside BLG.

In our calculations, we used $d_t = 80$ nm, $d_b = 50$ nm, $d = 0.335$ nm, and $\kappa_t = \kappa_b = 3.76$ (out-of-plane static dielectric constant of hexagonal boron nitride S28).

We use this parallel-plate capacitor model to find the electric potentials φ_{+S} , φ_{+C} and interlayer voltages φ_{-S} , φ_{-C} in the source region and in the channel in absence of ac signal, and also to calculate the channel response to an ac signal, see Supplementary Note 4.6. In the source region, there is only the bottom gate, while the role of a top gate is played by infinity, held at zero potential. This means $C_t = 0$, and the top gate disappears from the equations.

SUPPLEMENTARY NOTE 4.4: TUNNELING FIELD

In a TFET based on double-gated BLG, a tunnel junction is formed under the top gate edge, where the parallel-plate capacitor model of Supplementary Note 4.3 cannot be applied, and an accurate calculation of the tunneling field requires solving a two-dimensional electrostatic problem. This problem can be solved analytically in the absence of BLG S29, and the answer is

$$\tilde{E}_x = \frac{1 - \tilde{\varphi}}{[1 + \tilde{y}(1 - \tilde{\varphi}) \cot \tilde{y}\tilde{\varphi}]^2 + \tilde{y}^2(1 - \tilde{\varphi})^2}, \quad (\text{S19})$$

where

$$\tilde{E}_x \equiv \frac{E_x d_{tb}}{\pi [\varphi(x = -\infty) - \varphi(x = +\infty)]}, \tilde{y} \equiv \frac{\pi y}{d_{tb}}, \tilde{\varphi} \equiv \frac{\varphi - \varphi(x = -\infty)}{\varphi(x = +\infty) - \varphi(x = -\infty)} \quad (\text{S20})$$

are the dimensionless field in the plane of BLG, dimensionless position of BLG with respect to the gates ($\tilde{y} = 0$ at the bottom gate and π at the top gate), and dimensionless electric potential at the point where the field is calculated. $d_{tb} = d_t + d_b + d$ is the distance between gates, $\varphi(x = -\infty) = V_{bg}$ and $\varphi(x = +\infty) = V_{bg} + (y/d_{tb})(V_{tg} - V_{bg})$ are the electric potential in the source region and in the channel. The top and bottom dielectrics are assumed to be the same, as in our experiment.

Across a wide range of \tilde{y} , \tilde{E}_x is close to its low- \tilde{y} limit

$$\tilde{E}_x \approx \tilde{\varphi}^2 (1 - \tilde{\varphi}). \quad (\text{S21})$$

In the presence of BLG, exact calculation of the tunneling field would require solving the two-dimensional electrostatic problem numerically. To avoid this, we notice that adding BLG into the system reduces $\varphi(x = +\infty) - \varphi(x = -\infty)$ from several volts to tens or hundreds of millivolts. This suggests to approximate the screening by BLG via introducing a fictitious perfect conductor placed very close to the BLG. The potential of this conductor and its distance from the BLG are chosen so as to reproduce the correct potentials in the source and channel regions of BLG.

The resulting electric potential distribution in the system is shown in Supplementary Figure 7. Introducing the fictitious conductor allows us to keep Eq. (S21) for the electric field in BLG, if d_{tb} is replaced with d_t in the definition of (Eq. (S20)), and $\varphi(x = \pm\infty)$ are calculated in the parallel-plate capacitor model described in Supplementary Note 4.3.

Knowing the distribution of electric potential in BLG, we can calculate the tunnel current through the source-channel junction. Before we actually do this, we introduce two additional simplifications. First, we neglect field variations inside the barrier and assume tunneling through uniform field. This field is calculated at the point where the tunneling electron crosses the midgap ($E + e\varphi = 0$, where E is the electron energy). Second, instead of using different values of the tunneling field for electrons of different energies, we use a single value calculated for energy

$E = (E_{\text{tun,min}} + E_{\text{tun,max}})/2$. $E_{\text{tun,min}}$ and $E_{\text{tun,max}}$ are the boundaries of the energy region where tunneling is possible. Assuming zero temperature and both quasi-Fermi levels μ_S, μ_C in the source and the channel (near its beginning) lying within the band overlap region, we can write $E_{\text{tun,min}} = \min\{\mu_S, \mu_C\}$ and $E_{\text{tun,max}} = \max\{\mu_S, \mu_C\}$. (Remember that we are interested in the small-signal case, when the quasi-Fermi levels are close to each other and either lie both inside the band overlap region, or both outside. In the latter case, tunneling is impossible.)

To summarize, we use the following expression for the tunneling field:

$$F_{\text{tun}} \approx \frac{\pi |\varphi_{+C} - \varphi_{+, \text{tun}}|}{d_t} \left(\frac{\varphi_{+, \text{tun}} - \varphi_{+S}}{\varphi_{+C} - \varphi_{+S}} \right)^2, \quad (\text{S22})$$

where $\varphi_{+S}, \varphi_{+C}$ are calculated as described in [Supplementary Note 4.3](#), and $-e\varphi_{+, \text{tun}} = (\mu_S + \mu_C)/2$.

SUPPLEMENTARY NOTE 4.5: RESPONSIVITY OF THE SOURCE-CHANNEL JUNCTION

A zero-temperature ballistic expression for the tunnel current through the source-channel junction is

$$I_{\leftarrow s, \text{tun}} = 8eW \int_{\mu_C}^{\mu_S} \frac{dE}{2\pi\hbar} \int_{-k_{\perp \text{max}}(E)}^{k_{\perp \text{max}}(E)} \frac{dk_{\perp}}{2\pi} \mathcal{D}(E, k_{\perp}) \quad (\text{S23})$$

if $\mu_S > \mu_C$ (the opposite case is treated similarly). Here, $W = 6.2 \mu\text{m}$ is the channel width, $\mathcal{D}(E, k_{\perp})$ is the barrier transparency, the wavevector integral is taken up to the maximum possible transverse wavevector $k_{\perp \text{max}}(E)$ that an electron with energy E can have both in the source and in the channel, and the factor of 8 results from two spin projections, two valleys, and two tunneling paths in the imaginary k -space (interference between them^{S30} is neglected).

An analytical approximation can be derived by expanding the WKB barrier transparency in powers of k_{\perp} up to second order and extending the wavevector integration up to infinity^{S31}:

$$\begin{aligned} I_{\leftarrow s, \text{tun}} &\approx \frac{2e}{\pi^{3/2}\hbar} \mathcal{D}_{\text{tun}} k_{\perp \text{tun}} W (\mu_S - \mu_C), \\ \mathcal{D}_{\text{tun}} &\approx \exp \left(-\frac{\pi \sqrt{\gamma_1 E_{g, \text{tun}}^3}}{4\hbar v_0 e F_{\text{tun}}} \right), \\ k_{\perp \text{tun}} &\approx \sqrt{\frac{4}{\pi} \sqrt{\frac{\gamma_1}{E_{g, \text{tun}}}} \frac{e F_{\text{tun}}}{\hbar v_0}}. \end{aligned} \quad (\text{S24})$$

We assume that the transition between the source and the channel has the same shape for both the interlayer voltage and the electric potential and, therefore, the tunnel current flows through the bandgap $E_{g, \text{tun}} \approx |\varphi_{-, \text{tun}}|$, where

$$\frac{\varphi_{-, \text{tun}} - \varphi_{-S}}{\varphi_{-C} - \varphi_{-S}} = \frac{\varphi_{+, \text{tun}} - \varphi_{+S}}{\varphi_{+C} - \varphi_{+S}}. \quad (\text{S25})$$

At experimental conditions, the bandgap does not exceed 60 meV, so we use $E_g \approx |\varphi_-|$ instead of a more accurate expression (S12).

Expressions (S23), (S24) require that the chemical potentials μ_S, μ_C are taken at the points where the deviations of the carrier distributions from the Fermi-Dirac form are negligible. Since we consider the tunnel junction connected in series with the channel, we need an expression for the tunnel current in terms of the voltage *directly at the junction*, otherwise a certain part of the channel would be counted twice. This can be achieved by introducing a $1 - \mathcal{D}_{\text{tun}}$ correction in the denominator:

$$I_{\leftarrow s, \text{tun}} \approx \frac{2e}{\pi^{3/2}\hbar} \frac{\mathcal{D}_{\text{tun}}}{1 - \mathcal{D}_{\text{tun}}} k_{\perp \text{tun}} W (\mu_S - \mu_C), \quad (\text{S26})$$

similarly to the one-dimensional Landauer formula containing $\mathcal{D}/(1 - \mathcal{D})$ ^{S32, S33}.

The idealistic model that led to Eq. (S26) gives very small barrier transparency and huge tunnel resistance, orders of magnitude larger than in our experiment. This suggests there is some mechanism affecting the junction resistance, most likely electron-hole puddles, that create field fluctuations and may increase the average tunneling field. We take this effect into account phenomenologically, introducing a single fitting parameter F_{fluct} , which represents the average fluctuating field and is added to the tunneling field (S22) calculated without disorder:

$$\begin{aligned} I_{\leftarrow s, \text{tun}} &\approx \frac{2e}{\pi^{3/2}\hbar} \frac{\mathcal{D}_{\text{tun}}}{1 - \mathcal{D}_{\text{tun}}} k_{\perp \text{tun}} W (\mu_S - \mu_C), \\ \mathcal{D}_{\text{tun}} &\approx \exp \left(-\frac{\pi \sqrt{\gamma_1 E_{g, \text{tun}}^3}}{4\hbar v_0 e (F_{\text{tun}} + F_{\text{fluct}})} \right), \\ k_{\perp \text{tun}} &\approx \sqrt{\frac{4}{\pi} \sqrt{\frac{\gamma_1}{E_{g, \text{tun}}}} \frac{e (F_{\text{tun}} + F_{\text{fluct}})}{\hbar v_0}}. \end{aligned} \quad (\text{S27})$$

This is the final expression for the tunnel current that we used in our calculations. The value $F_{\text{fluct}} = 8 \text{ kV/cm}$ was found by fitting the experimental resistance in the tunnel regime and simultaneously gave responsivity in reasonable agreement with the experiment.

Assuming grounded source, $\mu_S = 0$, we identify μ_C with $-eV_{ss}$ and V_{tg} with V_{GS} from [Supplementary Note 4.1](#). Now, we can calculate the junction conductance as $G_S = -e\partial I_{\leftarrow s, \text{tun}}/\partial \mu_C$ and the intrinsic tunnel junction and tunnel-gate responsivities through (S6). When the doping types of source and channel are the same, or channel is undoped, there is no *tunnel* junction. In this case, we set the junction conductance to infinity and tunnel junction and tunnel-gate responsivities to zero.

SUPPLEMENTARY NOTE 4.6: RESPONSIVITY OF A LONG DOUBLE-GATED CHANNEL

In this section, we consider resistive self-mixing in a long^{S34} *double-gated* channel and find its responsivity. Our derivation closely follows that of Ref. S24, but extends it by (1) allowing the carrier density to depend separately on the top gate voltage and the Fermi level (because $\rho_+ = \rho_+ (\mu + eV_{tg})$ is no longer true in the presence of a bottom gate), (2) using frequency-dependent channel conductivity.

The basic assumptions of our model are that the dc channel conductivity $\sigma_{dc}(x, t)$ is instantaneously related to the local charge density $\rho_+(x, t)$, which, in turn, is related (also locally and instantaneously) to the top gate voltage $V_{tg}(t)$ and the Fermi level $\mu(x, t)$. Response to ac perturbations is described within the Drude model. Together with the charge conservation, we get a system of four equations:

$$\begin{aligned}\rho_+(x, t) &= \rho_+(V_{tg}(t), \mu(x, t)), \\ \frac{\partial J_{\leftarrow}(x, t)}{\partial t} &= -\frac{1}{e} \frac{\sigma_{dc}(x, t)}{\tau} \frac{\partial \mu(x, t)}{\partial x} - \frac{J_{\leftarrow}(x, t)}{\tau}, \\ \sigma_{dc}(x, t) &= \sigma_{dc}[\rho_+(x, t)], \\ \frac{\partial \rho_+(x, t)}{\partial t} &= \frac{\partial J_{\leftarrow}(x, t)}{\partial x},\end{aligned}\tag{S28}$$

with the boundary conditions of grounded source and zero drain current:

$$\mu(0, t) = 0, J_{\leftarrow}(+\infty, t) = 0.\tag{S29}$$

The top gate voltage consists of a constant bias and an ac signal, $V_{tg}(t) = V_{tg}^{(0)} + V_{in} \cos(\omega t)$. (Hereafter, quantities in the absence of the ac signal will be denoted by the ⁽⁰⁾ superscript, while next orders in V_{in} will be denoted by ⁽¹⁾ and ⁽²⁾, as in [Supplementary Note 4.1](#).)

To the first order in V_{in} , we obtain

$$\begin{aligned}\rho_+^{(1)} &= \frac{\partial \rho_+}{\partial V_{tg}} V_{in} + \frac{\partial \rho_+}{\partial \mu} \mu^{(1)}, \\ J_{\leftarrow}^{(1)} &= -\frac{1}{e} \frac{\sigma_{dc}^{(0)}}{1 - i\omega\tau} \frac{\partial \mu^{(1)}}{\partial x}, \\ \sigma_{dc}^{(1)} &= \frac{d\sigma_{dc}}{d\rho_+} \rho_+^{(1)}, \\ -i\omega\rho_+^{(1)} &= \frac{\partial J_{\leftarrow}^{(1)}}{\partial x}.\end{aligned}\tag{S30}$$

Using the boundary conditions (S29), we get the following solution

$$\begin{aligned}\mu^{(1)}(x) &= -\left(\frac{\partial \rho_+}{\partial \mu}\right)^{-1} \frac{\partial \rho_+}{\partial V_{tg}} V_{in} [1 - e^{iq_{pl}x}], \\ \rho_+^{(1)}(x) &= \frac{\partial \rho_+}{\partial V_{tg}} V_{in} e^{iq_{pl}x}, \\ J_{\leftarrow}^{(1)}(x) &= -\frac{1}{e} \frac{\sigma_{dc}^{(0)}}{1 - i\omega\tau} iq_{pl} \left(\frac{\partial \rho_+}{\partial \mu}\right)^{-1} \frac{\partial \rho_+}{\partial V_{tg}} V_{in} e^{iq_{pl}x}, \\ q_{pl} &\equiv \sqrt{\frac{i\omega(1 - i\omega\tau)}{\sigma_{dc}^{(0)}} \frac{\partial \rho_+}{\partial (-\mu/e)}}.\end{aligned}\tag{S31}$$

Having found the first-order current, we can write the channel “source-gate” conductance (W is the channel width):

$$\tilde{G}_{ch}(\omega) \equiv \frac{J_{\leftarrow}^{(1)}(0)W}{V_{in}} = -\frac{\sigma_{dc}^{(0)}}{1 - i\omega\tau} iq_{pl}W \left(\frac{\partial (-\mu/e)}{\partial V_{tg}}\right)_{\rho_+}.\tag{S32}$$

(Note that we use $\exp(-i\omega t)$ for the time dependence of harmonic signals instead of $\exp(+j\omega t)$ convention prevalent in electrical engineering, resulting in reactances having unconventional signs.)

The equation on the second order dc current results from the zero dc drain current condition,

$$J_{\leftarrow}^{(2)} = -\frac{1}{e} \sigma_{dc}^{(0)} \frac{\partial \mu^{(2)}}{\partial x} - \frac{1}{2e} \text{Re} \left(\sigma_{dc}^{(1)} \frac{\partial \mu^{(1)*}}{\partial x} \right) = 0,\tag{S33}$$

yielding the intrinsic channel responsivity

$$\begin{aligned}R_{ch,i} &\equiv \frac{V_{out}}{|V_{in}|^2/2} \equiv \frac{[\mu^{(2)}(+\infty) - \mu^{(2)}(0)]/(-e)}{|V_{in}|^2/2} \\ &= -\frac{1}{2} \left(\frac{\partial \ln \sigma_{dc}}{\partial V_{tg}} \right)_{\mu} \left(\frac{\partial (-\mu/e)}{\partial V_{tg}} \right)_{\rho_+}.\end{aligned}\tag{S34}$$

The expressions (S32), (S34), and the definition of q_{pl} (S31) differ from the results of Ref. S24 by two extra factors. The first factor $(\partial (-\mu/e)/\partial V_{tg})_{\rho_+}$ is unity in a single-gated FET and reduces to approximately $C_t/(C_t + C_b) = \tilde{d}_b/(\tilde{d}_t + \tilde{d}_b)$ in the presence of a bottom gate. The second factor $1/(1 - i\omega\tau)$ appears due to the frequency dependence of conductivity.

Calculations show that the difference between $(\partial(-\mu/e)/\partial V_{tg})_{\rho_+}$ and $\tilde{d}_b/(\tilde{d}_t + \tilde{d}_b)$ is minor and can be neglected within the accuracy of our model, so we used the following expressions for the channel “source-gate” conductance and intrinsic channel responsivity:

$$\begin{aligned}\tilde{G}_{\text{ch}}(\omega) &= -\frac{\sigma_{\text{dc}}^{(0)}}{1-i\omega\tau} i q_{\text{pl}} W \frac{\tilde{d}_b}{\tilde{d}_t + \tilde{d}_b}, \\ R_{\text{ch},i} &= -\frac{1}{2} \left(\frac{\partial \ln \sigma_{\text{dc}}}{\partial V_{tg}} \right)_{\mu} \frac{\tilde{d}_b}{\tilde{d}_t + \tilde{d}_b}, \\ q_{\text{pl}} &\equiv \sqrt{\frac{i\omega(1-i\omega\tau)}{\sigma_{\text{dc}}^{(0)}} \frac{\partial \rho_+}{\partial(-\mu/e)}}.\end{aligned}\tag{S35}$$

The derivatives in (S35) were evaluated with the help of the approximate electrostatic model presented in [Supplementary Note 4.3](#) and the constant-mobility approximation for the channel dc conductivity:

$$\sigma_{\text{dc}}^{(0)} = |\rho_+| \mu_{\text{BLG}} + \sigma_{\text{residual}}(V_{bg}),\tag{S36}$$

where we take $\mu_{\text{BLG}} = 10^5 \text{ cm}^2/(\text{V}\cdot\text{s})$ (according to measurements performed on similar devices^{S1}). The transport relaxation time τ was taken to be 2 ps according to the relation $\mu_{\text{BLG}} = e\tau/m^*$, where $m^* = \gamma_1/2v_0^2$ (this is the carrier effective mass in the band extrema of gapless BLG; in gapped BLG band dispersion is similar to the gapless case except in close vicinity of the band edges, so we neglect the bandgap dependence of m^*).

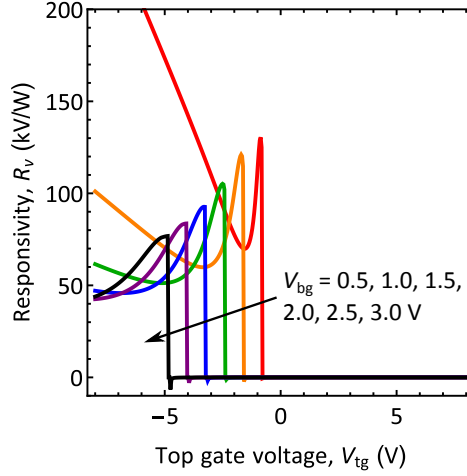
The residual conductivity σ_{residual} due to potential fluctuations in the channel was obtained by fitting the following formula to the experimental dc resistance at the channel neutrality point:

$$\frac{L}{W} \sigma_{\text{residual}}^{-1}(V_{bg}) = \frac{r_{\infty} V_{bg}^2 + r_0 V_0^2}{V_{bg}^2 + V_0^2}.\tag{S37}$$

The fitting procedure yielded $r_0 = 200 \Omega$, $r_{\infty} = 150 \text{ k}\Omega$, $V_0 = 5.5 \text{ V}$.

Using the intrinsic channel responsivity and channel “source-gate” conductance, together with the intrinsic tunnel junction and tunnel-gate responsivities and the tunnel junction conductance found in [Supplementary Note 4.5](#), we can obtain the total responsivity of our transistor through Eq. (S5) and convert it to the photodetector responsivity through Eq. (S9).

SUPPLEMENTARY NOTE 5: PERFORMANCE LIMITS OF BLG TFET PHOTODETECTORS



Supplementary Fig. 8 Responsivity of an ideal device. Calculated responsivity of our photodetector in absence of electric potential fluctuations.

The theory described in the previous Supplementary Sections was used to calculate the theoretical responsivity of our photodetector, which is shown in Fig. 4 of the main text. The detector responsivity in our theory is limited by the electric potential fluctuations and could be substantially improved in devices with reduced density of charged impurities. Supplementary Figure 8 shows the theoretical responsivity of our photodetector in absence of potential fluctuations (that is, with $F_{\text{fluct}} = 0$), which reaches hundreds kV/W.

Another way to increase detector responsivity is to exploit large nonlinearity of the tunnel junction at small values of band overlap (when the tunnel current is about to be switched off). This requires that the conduction band edge in the source region is simultaneously aligned with the valence band edge in the channel (or vice versa) and with the Fermi level.

Such kind of band alignment can be realized by introducing an additional gate above the source region and could potentially result in a very large nonlinearity even at room temperature^{S31}, which would yield infinite responsivity in the idealized model (no potential fluctuations, no leakage currents). This is easy to show by considering a power-law dependence of the tunnel conductance on the gate voltage, $G_S \propto (V_{tg} - V_{th})^\alpha$ for $V_{tg} > V_{th}$ and zero otherwise, which results from the power-law dispersion $k(E)$ near the band edges. Taking the logarithmic derivative of G_S with respect to the gate voltage, we obtain $|R_{TG,i}| = \alpha/(V_{tg} - V_{th})$ for nonzero α , or a δ -peak at $V_{tg} = V_{th}$ for $\alpha = 0$. A similar argument holds for $|R_{TJ,i}|$, since the band alignment is affected not only by the gate voltage, but also by the Fermi level in the channel.

In practice, the maximum achievable responsivity will be limited by potential fluctuations and leakage currents. Thermionic leakage hinders the performance of our detector at non-cryogenic temperatures because of the small bandgap (< 60 meV) realized in our TFET, but this problem can be mitigated by increasing the bandgap, either by applying a larger vertical field to BLG, or by using larger-gap materials, such as black phosphorus. Electric potential fluctuations present a more fundamental issue and limit the logarithmic derivatives of the tunnel conductance to $\sim 1/V_{\text{fluct}}$, where V_{fluct} is the magnitude of these fluctuations.

Assuming the total responsivity is dominated by R_{TJ} (as in our photodetector) and using equations (S5), (S6), and (S9), we can estimate the achievable room-temperature noise equivalent power as

$$\begin{aligned} \text{NEP}_{\min} &= \frac{\sqrt{4r_{2\text{pt}}k_B T}}{|R_v|} = \frac{\sqrt{4r_{2\text{pt}}k_B T}}{4Z_{\text{rad}} \left| \frac{Z_{\text{GS}}}{Z_{\text{GS}} + Z_{\text{rad}}} \right|^2 |R_{\text{TFET}}|} \approx \frac{\sqrt{4r_S k_B T}}{4Z_{\text{rad}} \left(\frac{r_S}{r_S + Z_{\text{rad}}} \right)^2 \frac{1}{2} \left| \frac{\partial \ln G_S}{\partial V_{SS}} \right|} \\ &\approx \frac{16}{9} \sqrt{3} V_{\text{fluct}} \sqrt{\frac{k_B T}{Z_{\text{rad}}}}, \end{aligned} \quad (\text{S38})$$

where $r_S = G_S^{-1}$ is the resistance of the source tunnel junction. To minimize the noise equivalent power, we assumed $r_S = 3Z_{\text{rad}}$, the drain junction is absent, and the channel resistance is negligible.

Taking $Z_{\text{rad}} = 75 \Omega$ and $V_{\text{fluct}} = 1$ mV (an experimentally achievable value^{S35}), we estimate that the room-temperature noise equivalent power in TFET-based photodetectors can be made as low as $0.02 \text{ pW}/\sqrt{\text{Hz}}$ (shown in Supplementary Figure 3).

SUPPLEMENTARY REFERENCES

- S1. Bandurin, D. A. *et al.* Resonant terahertz detection using graphene plasmons. *Nature Communications* **9**, 1–8 (2018).
- S2. SCONTEL. <http://www.scontel.ru>.
- S3. QMC Instruments Ltd. <http://www.terahertz.co.uk>.
- S4. Infrared Laboratories, Inc. <https://www.infraredlaboratories.com>.
- S5. Alsop, D. C., Inman, C., Lange, A. E. & Wilbanks, T. Design and construction of high-sensitivity, infrared bolometers for operation at 300 mK. *Applied Optics* **31**, 6610–6615 (1992).
- S6. Tanaka, S. T. *et al.* 100-mK bolometric receiver for low-background astronomy. In *Infrared Detectors and Instrumentation*, vol. 1946, 110–115 (International Society for Optics and Photonics, 1993).
- S7. Hubmayr, J. *et al.* Photon-noise limited sensitivity in titanium nitride kinetic inductance detectors. *Applied Physics Letters* **106**, 073505 (2015).
- S8. Monfardini, A. *et al.* A dual-band millimeter-wave kinetic inductance camera for the IRAM 30 m telescope. *The Astrophysical Journal Supplement Series* **194**, 24 (2011).
- S9. Kleinschmidt, P. *et al.* A highly sensitive detector for radiation in the terahertz region. *IEEE Transactions On Instrumentation and Measurement* **56**, 463–467 (2007).
- S10. Dai, J.-H., Lee, J.-H., Lin, Y.-L. & Lee, S.-C. In(Ga)As quantum rings for terahertz detectors. *Japanese Journal of Applied Physics* **47**, 2924 (2008).
- S11. Terasense Group, Inc. <https://terasense.com/>.
- S12. Vicarelli, L. *et al.* Graphene field-effect transistors as room-temperature terahertz detectors. *Nature Materials* **11**, 865–871 (2012).
- S13. Generalov, A. A., Andersson, M. A., Yang, X., Vorobiev, A. & Stake, J. A 400-GHz graphene FET detector. *IEEE Transactions on Terahertz Science and Technology* **7**, 614–616 (2017).
- S14. Bandurin, D. A. *et al.* Dual origin of room temperature sub-terahertz photoresponse in graphene field effect transistors. *Appl. Phys. Lett.* **112**, 141101 (2018).
- S15. Bauer, M. *et al.* A high-sensitivity AlGaIn/GaN HEMT terahertz detector with integrated broadband bow-tie antenna. *IEEE Transactions on Terahertz Science and Technology* **9**, 430–444 (2019).
- S16. Zagrajek, P. *et al.* Time resolution and dynamic range of field-effect transistor-based terahertz detectors. *Journal of Infrared, Millimeter, and Terahertz Waves* **40**, 703–719 (2019).
- S17. FerrerasMayo, M., Cibraite-Lukenskiene, D., Lisauskas, A., Grajal, J. & Krozer, V. Broadband sensing around 1 THz via a novel biquad-antenna-coupled low-NEP detector in CMOS. *IEEE Transactions on Terahertz Science and Technology* (2020).
- S18. Qin, H. *et al.* Detection of incoherent terahertz light using antenna-coupled high-electron-mobility field-effect transistors. *Applied Physics Letters* **110**, 171109 (2017).
- S19. Virginia Diodes, Inc. <https://www.vadiodes.com/>.
- S20. ACST GmbH. <https://acst.de/>.
- S21. Retzlöff, S. A., Young, A. & Hesler, J. L. A 1.46 THz Schottky receiver at cryogenic temperatures. In *2014 39th International Conference on Infrared, Millimeter, and Terahertz Waves (IRMMW-THz)*, 1–2 (IEEE, 2014).
- S22. Zhang, Z., Rajavel, R., Deelman, P. & Fay, P. Sub-Micron Area Heterojunction Backward Diode Millimeter-Wave Detectors With 0.18 pW/Hz^{1/2} Noise Equivalent Power. *IEEE Microwave and Wireless Components Letters* **21**, 267–269 (2011).
- S23. Rahman, S. M., Jiang, Z., Shams, M. I. B., Fay, P. & Liu, L. A G-band monolithically integrated quasi-optical zero-bias detector based on heterostructure backward diodes using submicrometer airbridges. *IEEE Transactions on Microwave Theory and Techniques* **66**, 2010–2017 (2017).
- S24. Sakowicz, M. *et al.* Terahertz responsivity of field effect transistors versus their static channel conductivity and loading effects. *Journal of Applied Physics* **110**, 054512 (2011).
- S25. Sanchez, A., Davis Jr, C. F., Liu, K. C. & Javan, A. The MOM tunneling diode: Theoretical estimate of its performance at microwave and infrared frequencies. *Journal of Applied Physics* **49**, 5270–5277 (1978).
- S26. Castro, E. V. *et al.* Electronic properties of a biased graphene bilayer. *Journal of Physics: Condensed Matter* **22**, 175503 (2010).
- S27. McCann, E. & Koshino, M. The electronic properties of bilayer graphene. *Reports on Progress in Physics* **76**, 056503 (2013).
- S28. Laturia, A., Van de Put, M. L. & Vandenberghe, W. G. Dielectric properties of hexagonal boron nitride and transition metal dichalcogenides: from monolayer to bulk. *npj 2D Materials and Applications* **2**, 1–7 (2018).
- S29. Maxwell, J. C. *A Treatise on Electricity and Magnetism*, vol. 1 (Clarendon press, 1873). Art. 202.
- S30. Nandkishore, R. & Levitov, L. Common-path interference and oscillatory Zener tunneling in bilayer graphene p-n junctions. *Proceedings of the National Academy of Sciences* **108**, 14021–14025 (2011).
- S31. Alymov, G., Vyurkov, V., Ryzhii, V. & Svintsov, D. Abrupt current switching in graphene bilayer tunnel transistors enabled by van Hove singularities. *Scientific Reports* **6**, 24654 (2016).
- S32. Datta, S. *Electronic Transport in Mesoscopic Systems* (Cambridge university press, 1997).
- S33. Strictly speaking, a proper averaging of $\mathcal{D}(E, k_{\perp})$ is required in the two-dimensional case. This is not an easy task, especially because we need not only linear, but also quadratic response, and the result will depend on the precise form of scattering that drives the carrier distributions toward equilibrium. This would anyway exceed the accuracy of our model, so we resort to this simple substitution. Its only role in our model is to provide smooth interpolation between the gapless case (unit transparency, there is essentially no tunnel junction, its conductance should become infinite), and the gapped case (small transparency, (S24) is applicable).
- S34. Our use of the long-channel approximation is motivated by the fact that the experimentally obtained plasmon resonances in responsivity are not as prominent as they are in the finite-channel theory. This suggests there are additional plasmon damping mechanisms not taken into account in our model, like interband absorption or effects of electron viscosity. Instead of complicating the model by considering them explicitly, we take into account the extra plasmon damping approximately, not by using a shorter decay length, but by setting the channel length to infinity.
- S35. Uwanno, T., Taniguchi, T., Watanabe, K. & Nagashio, K. Electrically inert h-BN/bilayer graphene interface in all-two-dimensional heterostructure field effect transistors. *ACS Applied Materials & Interfaces* **10**, 28780–28788 (2018).